Structure of differentiated planetesimals: a chondritic fridge on top of a magma ocean

Cyril Sturtz, Angela Limare, Marc Chaussidon, Édouard Kaminski

Highlights

Structure of differentiated planetesimals: a chondritic fridge on top of a magma ocean

Cyril Sturtz,Angela Limare,Marc Chaussidon,Édouard Kaminski

- We study the formation and the thermal evolution of planetesimals that accreted undifferentiated material during the first few Myr following the CAI formation.
- The protracted accretion of cold chondritic material results in the preservation of a few to tens of km thick undifferentiated crust on top of a magma ocean.
- Basal crustal melts rise in the crust where they stall and crystallize to produce andesitic rocks such as Erg Chech 002.

Structure of differentiated planetesimals: a chondritic fridge on top of a magma ocean[⋆,⋆⋆]

Cyril Sturtz[a,*], Angela Limare[a], Marc Chaussidon[a] and Édouard Kaminski[a]

[a]Université Paris Cité, Institut de Physique du Globe de Paris, CNRS, Paris, F-75005, France

ARTICLE INFO

Keywords:
Accretion
Planetesimals
Magma ocean
Meteorites
Erg Chech 002

ABSTRACT

Meteorites are interpreted as relics of early formed planetary bodies, and they provide information about the processes that occurred in the first few Myrs of our solar system. The ages measured for some differentiated meteorites (achondrites), indicate that planetesimals formed a differentiated silicate crust as early as ≈ 3 Myr after the beginning of the solar system. The composition of the recently discovered achondrite Erg Chech 002 (EC002), the oldest andesitic rock known so far, betokens partial melting of a chondritic source taking place as early as ≈ 1 Myr before all other known achondrites. However, thermal models of early accreted planetesimals predict massive melting of the planetesimal during core/mantle differentiation and cannot account for the preservation of a substantial amount of chondritic material. In this paper, we propose a way to interpret petrological and geochemical constraints provided by differentiated meteorites by introducing a refined thermal model of planetesimals formation and evolution. We demonstrate that continuous, protracted accretion of cold undifferentiated material upon a magma ocean over a timescale 2 times larger than the lifetime of the ^{26}Al heat source leads to the preservation of a few km thick chondritic crust. During accretion, the heat released by radioactive decay further induces episodes of partial melting at the base of the crust, which can led to the formation of andesitic rocks such as EC002. Using the available constraints on the age of EC002 and its cooling rate, the application of our model constraints the terminal radius of its parent body between 70 and 130 km.

1. Introduction

Meteorites are key witnesses of the processes that occurred during the first stages of planetary evolution. In particular, achondritic meteorites sample planetesimals differentiated during the first 5 Myr of the Solar system. Differentiated achondrites are often basaltic and most of them originate from a few parent bodies: the ureilites parent body, the angrites parent body, Vesta 4 - the eucrites parent body (Greenwood, Burbine and Franchi, 2020). Achondrites with andesitic or trachyandesitic compositions are very rare, e.g., GRA 06128 and 06129 (Day, Ash, Liu, Bellucci, III, McDonough, Walker and Taylor, 2009; Shearer, Burger, Neal, Sharp, Spivak-Birndorf, Borg, Fernandes, Papike, Karner, Wadhwa, Gaffney, Shafer, Geissman, Atudorei, Herd, Weiss, King, Crowther and Gilmour, 2010), Almahata Sitta ALM-A (Bischoff, Horstmann, Barrat, Chaussidon, Pack, Herwartz, Ward, Vollmer and Decker, 2014), NWA 11119 (Srinivasan, Dunlap, Agee, Wadhwa, Coleff, Ziegler, Zeigler and McCubbin, 2018) and NWA 11575 (Agee, Habermann and Ziegler, 2018). Recently, a new achondrite, Erg Chech 002 (EC002), has been recognized as the oldest andesitic meteorite known so far (Barrat, Chaussidon, Yamaguchi, Beck, Villeneuve, Byrne, Broadley and Marty, 2021).

Early Solar system relative chronology is anchored to the Ca-Al-rich inclusions (CAIs) from CV3 chondrites which are the oldest components of primitive chondrites according to U-Pb dating (Allègre, Manhès and Göpel, 1995; Bouvier and Wadhwa, 2010; Connelly, Bizzarro, Krot, Nordlund, Wielandt and Ivanova, 2012). The formation of CAIs is generally considered to date the episode of high-temperature condensation, or reprocessing of these condensates, which produced the first Solar system dust in the accretion disk. A crystallization age of 2.255 ± 0.015 Myr after CAIs have been inferred for EC002 from ^{26}Al –^{26} Mg chronology (Barrat et al., 2021), i. e. ≈ 1.2 Myr older than all other known achondrites, and contemporaneous with the formation of the metallic cores of the parent bodies of iron

⋆ This study contributes to the IdEx Université de Paris ANR-18-IDEX-0001.

⋆⋆ This work was supported by the Programme National de Planétologie (PNP) of CNRS/INSU, co-funded by CNES.

sturtz@ipgp.fr (C. Sturtz)

ORCID(s): 0000-0002-6329-949 (C. Sturtz); 0000-0001-6755-9843 (A. Limare); 0000-0001-8475-0690 (M. Chaussidon); 0000-0001-6965-8482 (É. Kaminski)

meteorites (Kruijer, Touboul, Fischer-Gödde, Bermingham, Walker and Kleine, 2014; Kruijer, Burkhardt, Budde and Kleine, 2017). Petrological and geochemical data on the two major mineral phases in EC002 (pyroxene and plagioclase) indicate that (i) the parent melt of EC002 was produced by 25% partial melting of a source of chondritic composition at a temperature of $1224 \pm 20\,^{o}C$, (ii) the pyroxenes crystallized at $1186 \pm 25\,^{o}C$ and re-equilibrated chemically at around $960\,^{o}C$, (iii) the cooling of the rock or mush (crystal + melt) took place at $\approx 5\,^{o}C\,yr^{-1}$ between $1200\,^{o}C$ and $1000\,^{o}C$, no melt being present anymore at $1000\,^{o}C$, and (iv) finally the rock was quenched below $\approx 900\,^{o}C$ at a rate $0.1 - 1\,^{o}C\,day^{-1}$ (Barrat et al., 2021). Although the $^{26}Al - ^{26}Mg$ systematics does not allow to date precisely the episode of melting, a model age for melting between 0.95 Myr and 2.2 Myr (mean 1.4 Myr) after CAIs has been proposed (Barrat et al., 2021). Note that because the $^{26}Al - ^{26}Mg$ age dates physically the closure temperature of Mg diffusion in EC002 plagioclases, the true crystallization age of EC002 can even be slightly earlier than 2.2 Myr, depending on the cooling rate before the closure of the chemical exchanges. In fact, recent Mg isotopic mesurements on mineral separates yielded a $^{26}Al - ^{26}Mg$ crystallization age of 1.80 Myr. (Fang, Frossard, Boyet, Bouvier, Barrat, Chaussidon and Moynier, 2022).

Early differentiation of planetesimals, within the first ≈ 2 Myr of the Solar system, as witnessed by iron meteorites (Kruijer et al., 2014, 2017) and EC002 (Barrat et al., 2021), stems from partial melting caused by the heat released by the radioactive decay of short lived ^{26}Al (and possibly ^{60}Fe). Intense radioactive internal heating can indeed induce several phenomena such as partial melting of chondritic materials (Elkins-Tanton, Weiss and Zuber, 2011), solid-state convection (Tkalcec, Golabek and Brenker, 2013; Kaminski, Limare, Kenda and Chaussidon, 2020), iron melt segregation (Neumann, Breuer and Spohn, 2012, 2014), core-mantle differentiation (Sahijpal, Soni and Gupta, 2007), magma ocean episodes (Greenwood, Franchi, Jambon and Buchanan, 2005), and volcanism (Mandler and Elkins-Tanton, 2013; Fu and Elkins-Tanton, 2014). Although the production mechanism of achondritic basaltic or andesitic magmas is still the object of debate, it must rely on the presence of a stable crust, either a primary or a secondary one, at the surface of the planetesimal (Taylor, 1989; Condie, 2016). Primary crusts are formed at the surface of a cooling magma ocean through the flotation of positively buoyant crystals from the magma ocean such as silica (Faure, 2020) or plagioclase that formed the anorthosite crust of the Moon (Wood, Dickey, Marvin and Powell, 1970; Warren, 1985). Partial melting of this primary crust can further lead to the formation of a basaltic secondary crust (Mandler and Elkins-Tanton, 2013). However, the petrology and geochemistry of some differentiated meteorites, such as EC002, indicate that their parent liquids formed directly from chondritic material at shallow depth in planetesimals. The metasomatic minerals found in the CO and CV chondrites (Ganino and Libourel, 2017) could be considered as products resulting from the first step of the thermal heating that could have later induced this partial melting.

An additional argument for the presence of a stable chondritic crust in planetesimals is the paleomagnetic record of a magnetic field in the parent body of primitive meteorites which implies both a core – hence a differentiated body – and preserved, undifferentiated, chondritic material. Thermal models of planetesimals available in the literature fail to account for the preservation of a chondritic crust in differentiated planetesimals (Weiss and Elkins-Tanton, 2013). Only few studies specifically considered the link between the thermal evolution of a planetesimal and its accretion history advocating that chondrites and achondrites can originate from the same parent body. For instance, Neumann et al. (2012) considered accretion by radial growth and modeled the differentiation of planetesimals by Darcy flow. They showed that the degree of differentiation varies significantly as a function of the accretion history. Kaminski et al. (2020) introduced a new accretion model for parent bodies of iron meteorites accounting both for planetesimals differentiation and chondritic crust preservation. Their thermal model took into account solid-state convection, but did not consider explicitly the possibility of generating a magma ocean episode. Dodds, Bryson, Neufeld and Harrison (2021) also proposed that crust constituents can be supplied by accretion of undifferentiated material, and considered the possibility of solid-state convection, followed by a magma ocean episode. But their model still predicts metamorphism of the chondritic material in the crust even though they allowed accretion to start relatively late (0.8 Myr) in order to mitigate heating.

In the present paper, we introduce and model a refined accretion and differentiation scenario that explains the preservation of a chondritic crust, and produces a thermal record consistent with geochemical and petrological evidences provided by some meteorites. As an illustration of the model predictions, we consider the particular case of the andesite EC002.

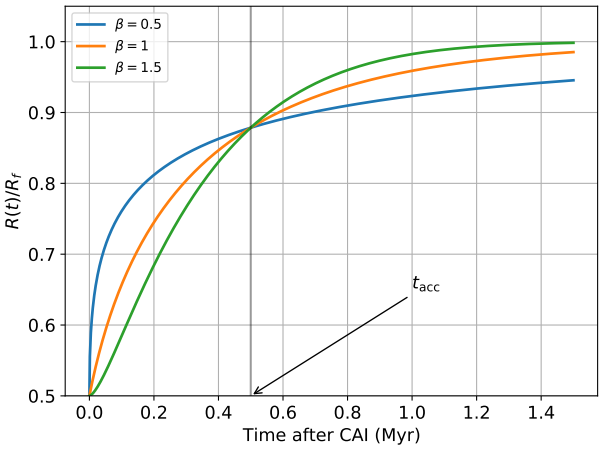

Figure 1: Accretion curves giving the evolution of the normalized radius of planetesimals (with $R_0/R_f = 0.5$ and $t_{acc} = 0.4$ Myr) for three values of the parameter β: $\beta = 0.5$ (red line), the typical value used in the model, $\beta = 1$ (blue line) corresponding to an exponential law, and $\beta = 1.5$ (purple line). The grey vertical line corresponds to t=$t_{acc} = 0.4$ Myr.

2. Thermal regimes and radial structures of accreting planetesimals

As inferred from petrological data, EC002 was formed by $\approx$ 25% partial melting of a chondritic source (Barrat et al., 2021). In the following, we establish in which conditions chondritic material can be preserved in a differentiated planetesimal.

2.1. Accretion

Planetesimals are supposed to form by the accretion of cold dust and pebbles in the mid-plane of the accretion disk (Visser and Ormel (2016); Johansen and Lambrechts (2017)). Processes such as turbulence in the disk can produce locally strong concentrations reaching thresholds that trigger quasi-instantaneous accretion of $\approx$ 100 km size planetesimals (Johansen, Oishi, Low, Klahr, Henning and Youdin, 2007; Cuzzi, Hogan and Shariff, 2008) thus bypassing the so-called meter-size barrier (Weidenschilling, 1977). In such a scenario, most planetesimals should be born big, as also suggested by simulations of the formation of embryos from planetesimals (Morbidelli, Bottke, Nesvorný and Levison, 2009). These accretion thresholds can theoretically be reached at various times and locations in the disk, depending on the availability and concentration of dust and pebbles. Hf $-$ W ages of iron meteorites indicate that their parent bodies accreted over the first 1.5 Myr of the solar system, whereas the accretion of the parent bodies of achondrites and chondrites was probably completed within the first $4-5$ Myrs (Kleine, Budde, Burkhardt, Kruijer, Worsham, Morbidelli and Nimmo, 2020). In the inner regions of the accretion disk, within the orbit of Jupiter, primordial dust can be rapidly exhausted, within a Myr or so, because of the barrier to dust migration from the outer disk created by the early formation of Jupiter (Morbidelli, Lambrechts, Jacobson and Bitsch, 2015; Haugbølle, Weber, Wielandt, Benítez-Llambay, Bizzarro, Gressel and Pessah, 2019). However, accretion of planetesimals can continue after 1 Myr since the flux of pebbles is never totally suppressed even for a fully-grown Jupiter.

In the following, we consider that growth of planetesimals can, in some cases, continue after the quasi-instantaneous accretion of a nucleus of several tens of km size (Kaminski et al., 2020). We further choose a Weibull accretion law to parametrize protracted accretion. The radius of the rocky body $R(t)$ grows from R_0 to the terminal radius R_f according to:

$$R(t) = R_f \left[1 - \left(1 - \left[\frac{R_0}{R_f}\right]^3\right) e^{-(t/t_{\rm acc})^\beta}\right]^{1/3}, \quad (1)$$

with $t_{\rm acc}$ the characteristic accretion timescale and β a constant. Equation (1) will be referred as the "protracted accretion" law hereafter. Three families of accretion scenarios can be defined as a function of the value of β (Figure 1). First, $\beta = 1$ corresponds to a specific case described simply by an exponential law. For $\beta < 1$, the planetesimal accretes material more rapidly than an exponential law at early times ($t < t_{acc}$) and supplied material more slowly at

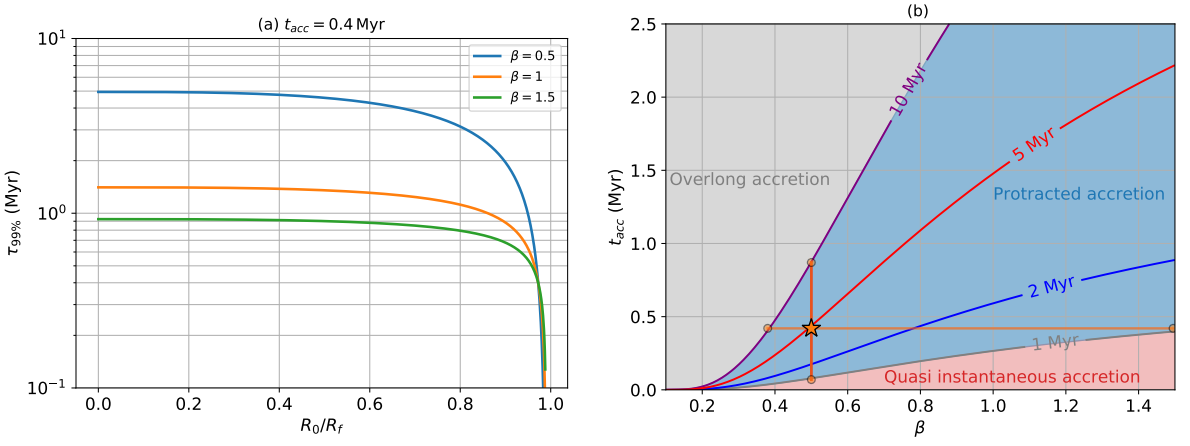

Figure 2: (a): Influence of R_0/R_f on the accretion timescale $\tau_{99\%}$. (b): Diagram showing the three families of accretion history as a function of the parameters t_{acc} and β. Each solid line represents an iso-value of $\tau_{99\%}$. "Quasi instantaneous accretion" stands for planetesimals whose accretion timescale $\tau_{99\%}$ is smaller than the lifetime of ^{26}Al ($t^{Al}_{1/2}/\ln 2$=1 Myr). "Overlong accretion" represents accretion which could take place in debris disk since $\tau_{99\%}$ is greater than the dissipation of the accretion disk ($\approx$ 10 Myr). The red star corresponds to the typical parameters of the accretion law used in the model (t_{acc}=0.4Myr and β=0.5). The orange points correspond to the extreme values of the accretion law used in the sensitivity study, in section 3.5.

$t > t_{acc}$, so that the terminal radius is reached later in the history of the planetesimal. For $\beta > 1$, the early accretion is slower than an exponential law at early time but material is brought more efficiently for $t > t_{acc}$ and the terminal radius is reached earlier in the planetesimal history.

We define the characteristic timescale of this law $\tau_{99\%}$ as the time at which the planetesimal radius reaches 99% of the terminal radius. After some developments, $\tau_{99\%}$ writes:

$$\tau_{99\%} = t_{acc} \left[\ln \left(\frac{1 - (R_0/R_f)^3}{0.03} \right) \right]^{1/\beta} \tag{2}$$

The accretion timescale $\tau_{99\%}$ is a function of the three parameters of the Weibull law. In figure 2 (a), the variation of $\tau_{99\%}$ with R_0/R_f shows that for R_0/R_f in the range $0 - 80\%$, the accretion timescale remains stable. For $R_0/R_f > 80\%$, the accretion timescale decreases dramatically, and the planetesimal undergoes a quasi-instantaneous accretion. Within this domain ($0\% < R_0/R_f < 80\%$) only t_{acc} and β have an influence on the accretion history.

Moreover, we can add two constraints on $\tau_{99\%}$. First, accretion has to be consistent with the lifetime of protoplanetary disk. Gas giants like Jupiter may have formed during the first Myr after CAI (Kruijer et al., 2017), and the dissipation of the solar nebula can range from a few to 10 Myr (Karl E. Haisch, Lada and Lada, 2001). We thus consider that $\tau_{99\%}$ has to be smaller than 10 Myr. Second, we compare the accretion timescale to the characteristic timescale of radioactive decay of ^{26}Al. If $\tau_{99\%} \ll t^{Al}_{1/2}/\ln 2$, accretion can be considered instantaneous ($R(t) \approx R_f$) and the content of radioactive ^{26}Al, hence the heating rate in the planetesimal are maximal. This case happens for $R_0/R_f \to 1$ and for small values of t_{acc}. Following these two constrains, we provide an abacus showing three families of accretion history in Figure 2 (b) : (i) when $\tau_{99\%} < 1$ Myr, accretion is considered quasi instantaneous, (ii) when $\tau_{99\%} > 10$ Myr, the accretion is too long compared to the lifetime of the disk, (iii) when $\tau_{99\%}$ is between these two end-members, the accretion is called "protracted".

2.2. Composition

We consider that the accreted undifferentiated chondritic material is a binary mixture of iron and silicates, with a mass fraction $x_{\rm Fe}$ and $x_{\rm Sil}$, respectively. The average density of the undifferentiated material ρ is:

$$\frac{1}{\rho} = \frac{x_{\rm Fe}}{\rho_{\rm Fe}} + \frac{x_{\rm Sil}}{\rho_{\rm Sil}}, \tag{3}$$

with ρ_i the density of phase i. We consider that melt crystallization can generate two types of crystals, one that is negatively buoyant relative to the melt (called H hereafter) and one that is positively buoyant relative to the melt (called L hereafter). The later produces a flotation crust at the top of the magma ocean, whereas the first induces the formation of a cumulate at the core-mantle boundary (CMB). The relative proportion of the two families of crystal is $\phi_{\mathrm{L},0}/\phi_{\mathrm{H},0} = 10/90$. This ratio is based on the proportion of plagioclase crystals relative to olivine and pyroxene crystals measured in some chondrites (Weisberg, Boesenberg, Kozhushko, Prinz, Clayton and Mayeda, 1995). Crystals L and H are effective "mineralogical phases" that provide a simplified description of the more complex mineral assemblages present in chondrites. As a consequence, L and M minerals are characterized by a solidus and a liquidus temperature. Between the solidus and the liquidus, the solid fraction in the melt, ϕ_{cr} (in vol%), is given by:

$$\phi_{cr} = \phi_{L,cr} + \phi_{H,cr}, \tag{4}$$

$$\phi_{L,cr} = \phi_{\mathrm{L},0}\,\frac{T_l^{\mathrm{L}} - \overline{T}}{T_l^{\mathrm{L}} - T_s^{\mathrm{L}}}, \tag{5}$$

$$\phi_{H,cr} = \phi_{\mathrm{H},0}\,\frac{T_l^{\mathrm{H}} - \overline{T}}{T_l^{\mathrm{H}} - T_s^{\mathrm{H}}}, \tag{6}$$

where $\overline{T}$ is the volume averaged bulk temperature in the planetesimal, T_l^i and T_s^i are the liquidus and the solidus temperature of mineral i, respectively, and $\phi_{i,0}$ its initial proportion (in vol%), and $\phi_{i,cr}$ the proportion of crystal i.

2.3. Thermal regime: from conduction regime to solid-state convection

2.3.1. Conduction regime

The bulk energy budget of undifferentiated planetesimal of radius $R(t)$ leads to the following equation (Kaminski et al., 2020) :

$$\rho c_p \frac{\mathrm{d}\overline{\mathrm{T}}}{\mathrm{dt}} = H_0 - \frac{3}{R}\,Q_s - \rho c_p\,\frac{3\overline{T}}{R}\,\frac{\mathrm{dR}}{\mathrm{dt}}, \tag{7}$$

with $c_p = x_{Fe}\,c_{p,Fe} + x_{Sil}\,c_{p,Sil}$ the planetesimal average heat capacity, H_0 the total rate of internal heating, and Q_s the surface heat flux. In equation (7), the dR/dt term corresponds to the effect of accretion of cold material on the thermal evolution of the planetesimal. Internal heating rates by radioactive elements ^{26}Al and ^{60}Fe are given by:

$$H_{0,\mathrm{Fe}} = \rho\,F_{\mathrm{Fe}}\left[\frac{^{60}\mathrm{Fe}}{^{56}\mathrm{Fe}}\right]_0 \frac{\ln 2}{t_{1/2}^{\mathrm{Fe}}}\,\mathcal{E}_{\mathrm{Fe}}\,e^{-t\ln 2/t_{1/2}^{\mathrm{Fe}}}, \tag{8}$$

$$H_{0,\mathrm{Al}} = \rho\,F_{\mathrm{Al}}\left[\frac{^{26}\mathrm{Al}}{^{27}\mathrm{Al}}\right]_0 \frac{\ln 2}{t_{1/2}^{\mathrm{Al}}}\,\mathcal{E}_{\mathrm{Al}}\,e^{-t\ln 2/t_{1/2}^{\mathrm{Al}}}, \tag{9}$$

where F_i is the chondritic abundance of i, $[i/j]_0$ is the initial abundance of radioactive and stable isotopes i and j, $\mathcal{E}_i$ is the decay energy per atom, $t_{1/2}^i$ the half-life.

As the planetesimal melts, latent heat is consumed, and likewise, when it crystalizes, latent heat is released. Outside the solidus to liquidus temperature interval, latent heat is zero. When the temperature falls within the solidus and the liquidus, latent heat contributes to the energy budget as an additional internal heat source quantified as:

$$H_{\mathrm{LH,Fe},0} = -L_{\mathrm{Fe}}\,x_{\mathrm{Fe}}\,\rho\,\frac{\mathrm{d}\overline{\mathrm{T}}}{\mathrm{dt}}\,\frac{1}{T_l^{\mathrm{Fe}} - T_s^{\mathrm{Fe}}}, \tag{10}$$

$$H_{\mathrm{LH,Sil},0} = -L_{\mathrm{Sil}}\,x_{\mathrm{Sil}}\,\rho\,\frac{\mathrm{d}\overline{\mathrm{T}}}{\mathrm{dt}}\,\frac{1}{T_l^{\mathrm{Sil}} - T_s^{\mathrm{Sil}}}, \tag{11}$$

with L_i the latent heat of component i (iron or silicate). The total rate of internal heating is thus $H_0 = H_{0,\mathrm{Al}} + H_{0,\mathrm{Fe}} + H_{\mathrm{LH,Sil},0} + H_{\mathrm{LH,Fe},0}$.

Our model considers the temperature at the surface of the body imposed by the temperature of the disk, which is a reasonably good approximation for planetesimals heated by ^{26}Al (Dodds et al., 2021), and is set to $T_s = 0\,^{\circ}\mathrm{C}$. At

Parameters	Symbols	Values	Units	Ref.
Iron content (mass fraction)	$x_{\rm Fe}$	0.18	-	(4)
Silicate content (mass fraction)	$x_{\rm Sil} = 1 - x_{\rm Fe}$	0.82	-	(4)
Chondritic abundance (^{60}Fe)	$F_{\rm Fe}$	$2.14\,10^{24}$	$\rm kg^{-1}$	(1)
Chondritic abundance (^{26}Al)	$F_{\rm Al}$	$2.62\,10^{23}$	$\rm kg^{-1}$	(1)
Decay energy per atom (^{60}Fe)	$\mathcal{E}_{\rm Fe}$	$4.87\,10^{-13}$	J	(1)
Decay energy per atom (^{26}Al)	$\mathcal{E}_{\rm Al}$	$4.42\,10^{-13}$	J	(1)
Initial relative abundance (^{60}Fe)	$[^{60}{\rm Fe}/^{56}{\rm Fe}]_0$	10^{-8}	-	(2)
Initial relative abundance (^{26}Al)	$[^{26}{\rm Al}/^{27}{\rm Al}]_0$	$5\,10^{-5}$	-	(2)
Half-life (^{60}Fe)	$t^{Fe}_{1/2}$	2.6	Myr	(1)
Half-life (^{26}Al)	$t^{Al}_{1/2}$	0.717	Myr	(1)
Iron density	$\rho_{\rm Fe}$	7800	$\rm kg\,m^{-3}$	(4)
Silicate density	$\rho_{\rm Sil}$	3200	$\rm kg\,m^{-3}$	(4)
Crystal/melt drop of density	$\Delta\rho$	100	$\rm kg\ m^{-3}$	-
Iron thermal conductivity	$\lambda_{\rm Fe}$	50	$\rm W\,m^{-1}\,K^{-1}$	(4)
Silicate thermal conductivity	$\lambda_{\rm Sil}$	3	$\rm W\,m^{-1}\,K^{-1}$	(4)
Thermal expansion (Fe)	$\alpha_{\rm Fe}$	$7.7\,10^{-5}$	$\rm K^{-1}$	(1)
Thermal expansion (Silicate)	$\alpha_{\rm Sil}$	$2\,10^{-5}$	$\rm K^{-1}$	(1)
Specific heat (Silicate)	$c_{p,\rm Sil}$	1168	$\rm J\,K^{-1}\,kg^{-1}$	(3)
Specific heat (Fe)	$c_{p,\rm Fe}$	622	$\rm J\,K^{-1}\,kg^{-1}$	(3)
Latent heat (Fe)	$L_{\rm Fe}$	250	$\rm kJ\,kg^{-1}$	(4)
Latent heat (Silicate)	$L_{\rm Sil}$	500	$\rm kJ\,kg^{-1}$	(4)
Liquidus (Fe)	$T_l^{\rm Fe}$	1615	°C	(4)
Solidus (Fe)	$T_s^{\rm Fe}$	990	°C	(4)
Liquidus (Silicate and chondritic mat.)	$T_l^{\rm Sil}$	1700	°C	(4)
Solidus (Silicate)	$T_s^{\rm Sil}$	1200	°C	(4)
Solidus light mineral	$T_s^{\rm L}$	1200	°C	(6)
Solidus heavy mineral	$T_s^{\rm H}$	1200	°C	(6)
Liquidus light mineral	$T_l^{\rm L}$	1350	°C	(6)
Liquidus heavy mineral	$T_l^{\rm H}$	1700	°C	(6)
Activation energy (Sil)	$E_{a,\rm Sil}$	250	$\rm kJ\,mol^{-1}$	(4)
Activation energy (Fe)	$E_{a,\rm Fe}$	13	$\rm kJ\,mol^{-1}$	(4)
Viscosity of iron melt at $T_l^{\rm Fe}$	η_0	1	Pa s	(3)
Melt fraction factor for silicate	σ_{Sil}	21	-	(4)
Melt fraction factor for iron	σ_{Fe}	4	-	(4)
Suspended crystals radius	r	3.10^{-3}	m	(5)

Table 1
Parameters used in the thermal model. References are the following : Neumann et al. (2014) (1), Tang and Dauphas (2012) (2), Neumann et al. (2012) (3), Kaminski et al. (2020) (4), Solomatov (2000) (5), adapted and simplified from Righter and Drake (1997) (6).

the early stages of the thermal evolution of the planetesimal, heat is evacuated by conduction and the surface heat flux can be calculated analytically (Carslaw and Jaeger, 1959). For an exponential internal heat generation source given by $H(t) = H_0 \exp(-\lambda t)$ with zero initial and surface temperatures, the surface heat flux is:

$$Q_s(t) = -\frac{\kappa H_0}{\lambda}\left[\sqrt{\frac{\lambda}{\kappa}}\tan^{-1/2}\left(R\sqrt{\frac{\lambda}{\kappa}}\right) - \frac{1}{R}\right]\exp(-\lambda t) - \frac{2RH_0}{\pi}\sum_{n=1}^{+\infty}\frac{\exp\left(-\frac{\kappa n^2\pi^2 t}{R^2}\right)}{n^2 - \frac{\lambda}{\kappa}\left(\frac{R}{\pi}\right)^2}. \quad (12)$$

Here we consider only the heat production by ^{26}Al with $\lambda = \ln 2/t^{\rm Al}_{1/2}$. Because conduction is not a very efficient heat transfer, the bulk temperature of the planetesimal increases, until new processes occur in the interior of the planetesimal.

2.3.2. Onset of solid-state convection

As heating proceeds, the planetesimal is bound to melt. Partial melting implies a strong decrease of viscosity and can generate instabilities of pure thermal origin or related to liquid iron percolation that trigger solid-state convection

at planetary scale (Kaminski et al., 2020). Convection is characterized by two dimensionless numbers (Roberts, 1967), the Rayleigh-Roberts number Ra^*_H that accounts for the vigor of convection, and the Prandtl number that quantifies the importance of inertia:

$$Ra^*_H = \frac{\alpha \rho g H^* R^5}{\kappa \eta \lambda}, \tag{13}$$

$$Pr = \frac{\nu}{\kappa}, \tag{14}$$

where α is the thermal expansion coefficient, $g = 4/3\pi \mathcal{G} \rho R$ is the surface gravity with $\mathcal{G}$ the gravitational constant, λ is the thermal conductivity, κ is the thermal diffusivity, η is the dynamic viscosity, $\nu = \eta/\rho$ is the kinematic viscosity, and H^* is the effective rate of internal heating that takes into account secular cooling (Limare, Jaupart, Kaminski, Fourel and Farnetani, 2019; Limare, Kenda, Kaminski, Surducan, Surducan and Neamtu, 2021):

$$H^* = H - \rho c_p \frac{\mathrm{d}\overline{\mathrm{T}}}{\mathrm{dt}}. \tag{15}$$

Convection starts if Ra^*_H is larger than the critical value $Ra_{H,c} = 5758$ (Schubert, Turcotte and Olson, 2001). In the case of a material whose viscosity is strongly temperature dependent, convection will develop under a stagnant lid after a delayed onset time τ_{SL} (Davaille and Jaupart, 1993). In the regime of solid-state convection, the heat budget of the convecting planetesimal is still given by equation (7) but with a surface heat flux now given by the scaling law (Davaille and Jaupart, 1993; Choblet and Sotin, 2000):

$$Q_s = \lambda \left(\frac{\alpha \rho g}{\kappa \eta} \right)^{1/3} \left(\frac{\Delta T_v}{C_T} \right)^{4/3}, \tag{16}$$

$$\Delta T_v = -C_v \eta / \frac{\mathrm{d}\eta}{\mathrm{dT}}, \tag{17}$$

where ΔT_v is the characteristic viscous temperature scale for convection with a stagnant lid, $C_v = 2.24$ (Davaille and Jaupart, 1993), and C_T a constant that depends on the mechanical boundary condition (here we will use $C_T = 3.31$ following Limare et al. (2021)). The continuity of the heat flux through the stagnant lid leads to the determination of its thickness δ_{SL}:

$$\delta_{SL}\left(\overline{T}\right) = \frac{R}{2}\left(1 - \sqrt{1 - \frac{4\lambda\left(\overline{T} - \Delta T_v - T_s\right)}{Q_s R}}\right), \tag{18}$$

where T_s is the surface temperature.

The scaling laws introduced above emphasizes the key influence of the viscosity on the dynamics of convection. In planetesimals, this issue is of peculiar importance because of the large variation of viscosity expected during the progressive heating of the material and its partial melting. For the silicate component we use a modified Arrhenius law to account for these dependencies (Scott and Kohlstedt, 2006; Kaminski et al., 2020):

$$\eta(\overline{T}, \phi_{cr}) = \eta_0 \, f(\phi) \, \exp\left[\frac{E_{a,\mathrm{Sil}}}{R_g}\left(\frac{1}{\overline{T}} - \frac{1}{T_0}\right)\right], \tag{19}$$

$$f(\phi_{cr}) = \exp\left[-\sigma_{\mathrm{Sil}}(1 - \phi_{cr})\right]. \tag{20}$$

where $f(\phi_{cr})$ encompasses the influence of partial melting on the viscosity, η_0 is the reference viscosity at $T_0 = 1000^{\mathrm{o}}\mathrm{C}$, $E_{a,\mathrm{Sil}}$ the activation energy for silicates and R_g the ideal gas constant. Because the amount of melt is related to the temperature, the variation of viscosity with temperature is amplified, and the convection may further transition to a magma ocean episode, as explained below.

2.4. Magma ocean episode

2.4.1. Rheological transition: magma ocean and core formation

At a certain degree of melting, the solid matrix becomes unstable and the behavior of the mixture becomes that of a suspension of solid crystals in a liquid magma (Solomatov, 2000). The type of convection changes at rheological

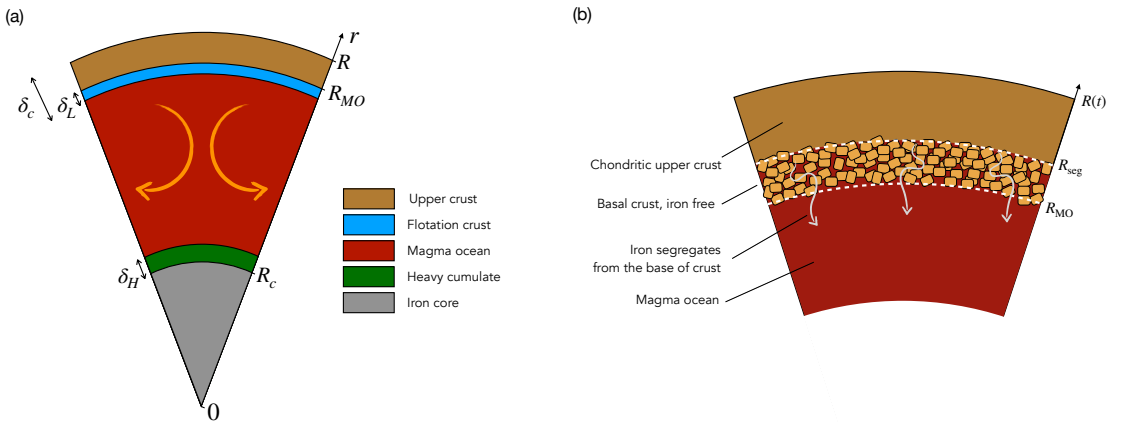

Figure 3: (a) Illustration of the stratification inside a planetesimal during a magma ocean episode. (b) Illustration of the iron-silicate differentiation that occurs at the base of the crust. Between $R(t)$ and $R_{\rm seg}$, the crust remains cold and chondritic. Between $R_{\rm seg}$ and R_{MO}, the crust temperature is high enough to trigger iron-silicate segregation. Iron is drained, and the remaining crust is made of silicate component only. As iron leaves, the lower part of the crust thins.

transition $\phi_{\rm RT} = 60\%$ (Elkins-Tanton, 2012; Guazzelli and Pouliquen, 2018), from laminar solid state convection to liquid-like, turbulent convection. In the so called "magma ocean" regime, the viscosity law (19) is modified so that $f(\phi)$ is now expressed by a Krieger-Dougherty law (Krieger and Dougherty, 1959):

$$f(\phi) = \left(1 - \frac{\phi}{\phi_c}\right)^{-2.5\phi_c}, \tag{21}$$

where ϕ stands for the volume fraction of crystals in suspension, whereas ϕ_{cr} is the total amount of crystals in the mantle, either in suspension or settled. We set ϕ_c at 60.002% to ensure the continuity of the viscosity at $\phi = \phi_{\rm RT}$ and to reach a viscosity of 14 Pa s for purely liquid magma, consistent with the estimates of Rubie, Melosh, Reid, Liebske and Righter (2003). The variation of the viscosity as a function of the temperature is given in Appendix 2.4.1 assuming an equilibrium melting.

Beyond the rheological transition, the viscosity is reduced by a few orders of magnitude and opens the way to metal extraction (Sturtz, Limare, Tait and Kaminski, 2021c). As a matter of fact, before the rheological transition, the planetesimal is a mush with a low degree of partial melting and iron migration to the center of the planetesimal occurs by porous flow (Neumann et al., 2012). The timescale for iron to reach the center of the planetesimal is $1 - 10$ Myr, which is long compared to the time required for the onset of the magma ocean (less than 1 Myr, as it will be discussed later). Hence we assume that no metal-silicate segregation happened before the rheological transition. On the other hand, once the rheological transition has been reached, there is no more matrix resistance to the iron migration and we consider that it happens instantaneously (Höink, Schmalzl and Hansen, 2006).

A second important consequence of the low viscosity of the convective fluid once the rheological transition has been reached is the potential development of relative motions between melt and crystals, and ultimately the possibility of forming layers of segregated crystals: cumulate of thickness δ_H can grow by deposition of the heavy crystals at the core-mantle boundary (CMB), whereas a layer of light crystals can accumulate below the chondritic material brought at the surface of the planetesimal, the two contributions forming a crust of total thickness δ_c, as drawn in Figure 3 (a).

2.4.2. Thermal state of the bulk magma ocean and the core

The magma ocean is treated as a convecting shell. Through the introduction of a geometrical factor for the silicate, convecting mantle:

$$f_c = \frac{R_c}{R_{\rm MO}} = \left(\frac{\rho}{\rho_{\rm Fe}}\, x_{\rm Fe}\right)^{1/3}, \tag{22}$$

where R_c is the core radius and R_{MO} is the distance between the top of the magma ocean and the center of the planetesimal (figure 3(a)). With parameters summarized in Table 1, $f_c = 0.42$ right after the core differentiation.

The energy budget for the magma ocean and for the core are:

$$\rho_{\rm Sil} c_{p,\rm Sil} \frac{{\rm dT_{MO}}}{{\rm dt}} = H_{\rm MO} + H_{\rm LH,Sil} + Q_{\rm CMB} \frac{S_c}{V_m} - Q_s \frac{S_m}{V_m}, \quad (23)$$

$$\rho_{\rm Fe} c_{p,\rm Fe} \frac{{\rm dT_c}}{{\rm dt}} = H_c + H_{\rm LH,Fe} - Q_{\rm CMB} \frac{S_c}{V_c}, \quad (24)$$

where $T_{\rm MO}$ and T_c are the bulk average temperatures of the magma ocean and of the core, respectively, $Q_{\rm CMB}$ is the heat flux at the CMB, $S_m = 4\pi R^2 \left[1-(\delta_c/R)^2\right]$ the top surface area of the magma ocean, $V_m = 4/3\pi R^3 \left[(1-\delta_c/R)^3 - (f_c\{1-\delta_c/R\} + \delta_H/R)^3\right]$ the volume of the magma ocean, $S_c = 4\pi f_c^2 R^2 (1-\delta_c/R)^2$ the surface area of the core and $V_c = 4/3\pi R^3 f_c^3 (1-\delta_c)^3$ its volume.

As Al is highly lithophile, we assume that all ^{26}Al is fully partitioned into the magma ocean. On the other hand, we consider that all iron is partitioned into the core, hence that no ^{60}Fe is present in the magma ocean. Accordingly, the rate of internal heating in each reservoir can be written by modulating (8)-(11) by a concentration factor:

$$H_c = H_{0,\rm Fe} f_c^{-3} \left(1 - \frac{\delta_c}{R}\right)^{-3}, \quad (25)$$

$$H_{\rm MO} = H_{0,\rm Al} \left[\left(1-\frac{\delta_c}{R}\right)^3 - \left(f_c\left\{1-\frac{\delta_c}{R}\right\} + \frac{\delta_H}{R}\right)^3\right]^{-1}, \quad (26)$$

whereas the release of latent heat in the two reservoirs is given by:

$$H_{\rm LH,Fe} = -L_{\rm Fe}\,\rho_{\rm Fe} \frac{{\rm dT_c}}{{\rm dt}} \frac{1}{T_l^{\rm Fe} - T_s^{\rm Fe}}, \quad (27)$$

$$H_{\rm LH,Sil} = -L_{\rm Sil}\,\rho_{\rm Sil} \frac{{\rm dT_{MO}}}{{\rm dt}} \frac{1}{T_l^{\rm Sil} - T_s^{\rm Sil}}. \quad (28)$$

The potential presence of a crust at the surface of the magma ocean and at the CMB yields expressions for the heat fluxes that are more complex than the classical scaling laws used for convective systems. The crust acts like a thermal insulator and the temperature at the base of the crust $T_{b,c}$ is linked to the convective heat flux through:

$$Q_s = \lambda_{\rm Sil} \left(\frac{\alpha_{\rm Sil}\rho_{\rm Sil} g}{\kappa_{\rm Sil}\eta}\right)^{1/3} \left(\frac{T_{\rm MO} - T_{b,c}}{C_T}\right)^{4/3}. \quad (29)$$

Furthermore, heat transfer occurs by conduction in the crust and follows Fourier's law (Jaupart and Mareschal (2010), pp.36):

$$Q_s = \lambda_{\rm Sil} \frac{T_{b,c} - T_s}{\delta_c(t)} \frac{R(t)}{R(t) - \delta_c(t)}. \quad (30)$$

At the beginning of the magma ocean episode, the crust is only composed of undifferentiated material brought by accretion. The presence of radioactive elements in the magma ocean later induces high temperatures close to the liquidus, which in turn lead to partial melting of the base of the crust. As silicates are more refractory than iron, the base of the crust is hot enough for iron melting to occur. Due to the high density contrast, liquid iron segregates from the base of the crust, and the crust is composed of a chondritic upper part, and an iron-depleted lower part (Figure 3 (b)). This consideration has two main consequences. First, when iron is extracted, the crust thickness decreases. Second, as the crustal thinning occurs at a temperature below the liquidus of silicate, the heat flux increases so the magma ocean cools at a sub-liquidus temperature. As in the previous section when dealing with the massive iron/silicate segregation, we consider the temperature at which the iron is supposed to be extracted from the crust as being the rheological temperature of silicates (1366°C).

Sturtz, Kaminski, Limare and Tait (2021a) developed a physical model establishing whether crystals formed during magma ocean cooling can be entrained by convection or not, based on a dimensionless parameter defined as the ratio

between the convective shear stress and the buoyancy of crystals. This dimensionless parameter is a modified Shields number that combines the convection parameters and the crystals characteristics:

$$\zeta = \frac{\kappa\eta}{h_{MO}^2 \Delta\rho g r} Ra_H^{*3/8}, \tag{31}$$

with r the crystal radius, $\Delta\rho$ the density difference between the crystals and the melt, and $h_{MO} = R[1 - \delta_c/R - \delta_H/R - f_c(1 - \delta_c/R)]$ the thickness of the magma ocean. If ζ is below a critical value ζ_c crystals are not entrained by the convection and they can deposit, whereas if $\zeta > \zeta_c$, convective flow can keep crystals in suspension (Shields, 1936; Charru, Mouilleron and Eiff, 2004). Sturtz et al. (2021a) validated this criterion experimentally for the formation of both cumulates and floating lids, and obtained $\zeta_c = 0.29 \pm 0.17$. In the present case, because the viscosity of the magma ocean is very low (i.e. liquid like), the Shields number falls well below the critical value.

At the CMB, the way heat is transported depends on the magma ocean temperature. In the initial stage of the magma ocean, its temperature increases by internal heating up to maximum values close to the silicate liquidus. In these conditions there is no crystal cumulate at the CMB, and we consider that the core is always well mixed and characterized by an average temperature. On the magma ocean side, a thermal boundary layer forms at the CMB. In the stagnant lid regime, the TBL thickness at the CMB $\delta_{\rm CMB}$ is linked to the stagnant lid thickness $\delta_{\rm SL}$ by (Solomatov, 1995; Bryson, Neufeld and Nimmo, 2019; Dodds et al., 2021):

$$\delta_{\rm CMB} = \delta_{\rm SL} \frac{\Delta T_v}{T_{\rm MO} - T_s}, \tag{32}$$

with $\Delta T_v = -C_v\eta/\partial_T\eta$ if $T_{\rm MO} > T_c$, and $\Delta T_v = -C_v\eta_{\rm Fe}/\partial_T\eta_{\rm Fe}$ if $T_{\rm MO} < T_c$. The CMB heat flux can then be expressed as a function of the surface heat flux as:

$$Q_{\rm CMB} = Q_s \frac{T_{\rm MO} - T_c}{\Delta T_v}. \tag{33}$$

As the magma ocean cools down, a cumulate of "heavy silicate crystals" can form at the CMB. As long as the cumulate thickness is thinner than the TBL thickness at the CMB, heat transfer between the core and the mantle occurs by convection and equation (33) remains valid. If the cumulate is thicker than the TBL, the conductive heat flux $Q_{\rm CMB}$ in given by:

$$Q_{\rm CMB} = \lambda_{\rm Sil} \frac{T_{b,\rm MO} - T_{\rm CMB}}{\delta_H(t)} \frac{R_c(t) + \delta_H(t)}{R_c(t)}, \tag{34}$$

where $T_{b,\rm MO}$ is the temperature at the base of the magma ocean, and $T_{\rm CMB}$ is the temperature at the surface of the core. If the magma ocean is hotter than the core, we assume that the core acts like a thermostat, and sets $T_{\rm CMB} = T_c$, whereas $T_{b,\rm MO}$ is obtained from the heat flux using the scaling law:

$$Q_{\rm CMB} = \lambda_{Fe} \left(\frac{\alpha_{\rm Sil}\rho_{\rm Sil} g_c}{\kappa_{\rm Sil}\eta}\right)^{1/3} \left(\frac{T_{\rm MO} - T_{b,\rm MO}}{C_T}\right)^{4/3}. \tag{35}$$

Similarly, if the the core is hotter than the magma ocean, we assume $T_{b,\rm MO} = T_{\rm MO}$, whereas the temperature $T_{\rm CMB}$ is obtained from the heat flux at the CMB given by:

$$Q_{\rm CMB} = \lambda_{Fe} \left(\frac{\alpha_{\rm Fe}\rho_{\rm Fe} g_c}{\kappa_{\rm Fe}\eta_{\rm Fe}}\right)^{1/3} \left(\frac{T_{\rm c} - T_{\rm CMB}}{C_T}\right)^{4/3}. \tag{36}$$

Within this framework, the thermal evolution of the system is totally determined by (23)-(24). However, two parameters are missing to solve this set of equations: the thickness of the crust δ_c and the thickness of the heavy cumulate δ_H.

2.4.3. Mechanical evolution of the crust and of the cumulate

At the surface, the crust is fed both by the accretion of chondritic material and by the flotation of light crystals from the magma ocean. The growth of the chondritic part of the crust follows the protracted accretion law (1) while

the thickening due to flotation of light crystals follows the law given by Sturtz, Limare, Tait and Kaminski (2021b). The total growth rate is then given by:

$$\frac{\mathrm{d}\delta_\mathrm{c}}{\mathrm{dt}} = \frac{\mathrm{dR}}{\mathrm{dt}} + c_d v_s \phi_L, \tag{37}$$

where ϕ_L is the volume fraction of light crystals in suspension in the magma ocean, v_s is the sedimentation velocity of these light crystals and c_d is a constant of order unity. Experiments in different types of convective systems have shown that for diluted suspensions v_s scales with Stokes' velocity (Martin and Nokes, 1988, 1989; Lavorel and Le Bars, 2009; Sturtz et al., 2021b). To take into account the influence of crystals concentration on the settling velocity v_s, we use the viscosity described in section 2.4.1, that takes into account the effect of temperature T and the effect of the suspension on the viscosity:

$$v_s = \frac{\Delta\rho g r^2}{\eta(T,\phi)}, \tag{38}$$

with $\Delta\rho$ the density difference between the melt and crystals, r the crystal radius, and ϕ the volume fraction of crystals in suspension.

When the MO temperature decreases below the silicate liquidus, heavy crystals nucleate, sink and form a cumulate at the CMB. The rate of thickening of this layer δ_H is given by:

$$\frac{\mathrm{d}\delta_\mathrm{H}}{\mathrm{dt}} = c_d v_s \phi_H, \tag{39}$$

with ϕ_H the volume fraction of heavy crystal in suspension in the magma ocean. Note that equations (37) and (39) are valid only when the magma ocean temperature is below the light and heavy silicate crystals melting temperature, respectively. If the magma ocean temperature is higher than their liquidus, the layers undergo melting, i.e., are thermally eroded.

3. Results - what was the size of EC002 parent body?

3.1. Necessity to take accretion into account

A magma ocean episode is consistent both with an efficient core formation by metal-silicate differentiation and with the preservation of an undifferentiated crust at the surface. Because EC002 analyses indicate an early accretion, we first consider a scenario in which its parent body accreted instantaneously at t_0 (Li, Youdin and Simon, 2019). Within the framework developed above, this scenario simply implies $\mathrm{dR/dt} = 0$ in equation (7). We solved numerically equation (7) using a finite difference scheme. As the conservation of energy is considered for the entire planetesimal, the physical parameters do not have a radial dependence. They are all volume averaged, for each reservoir, as underlined in equations 23 and 24. As a consequence, we only need a temporal discretization, and we use an order one explicit scheme. In the parameter space (R, t_0) we track the conditions required to produce a magma ocean episode. As shown in Figure 4 (a), a magma ocean occurs in a planetesimal of radius R if it accreted early enough. If the accretion takes place too late, the radioactive source is not sufficient to supply the required energy to reach the rheological transition.

Once the magma ocean episode has started (at ≈ 0.45 Myr for a 100 km body, accreted instantaneously at t_0=0), a chondritic crust remains at the surface as part of the stagnant lid with an initial thickness spanning from 0.5 to 1.5 km depending on the size of the planetesimal. However, as illustrated in Figure 4 (b), this crust is bound to undergo a first melting at ≈ 0.64 Myr that decreases its thickness. This is due to the fact that the crust insulates thermally the magma ocean where all ^{26}Al is essentially stored. Note that the crust also contains ^{26}Al, but the effects are negligible on the global budget. After this first melting episode, the chondritic reservoir that can be preserved at the surface has a very small thickness. For instance, for a R_f in the range of 50 to 500 km, the chondritic material can only be preserved in a $100 - 600$ m thick crust. Although the crust thickens at the end of the magma ocean episode by addition of light crystals segregated from the magma ocean, its chondritic part is not thick enough to survive foundering triggered by impacts (Hevey and Sanders, 2006; Elkins-Tanton et al., 2011). We thus conclude that EC002 cannot be explained by a scenario of instantaneous accretion and we now consider a scenario of protracted accretion.

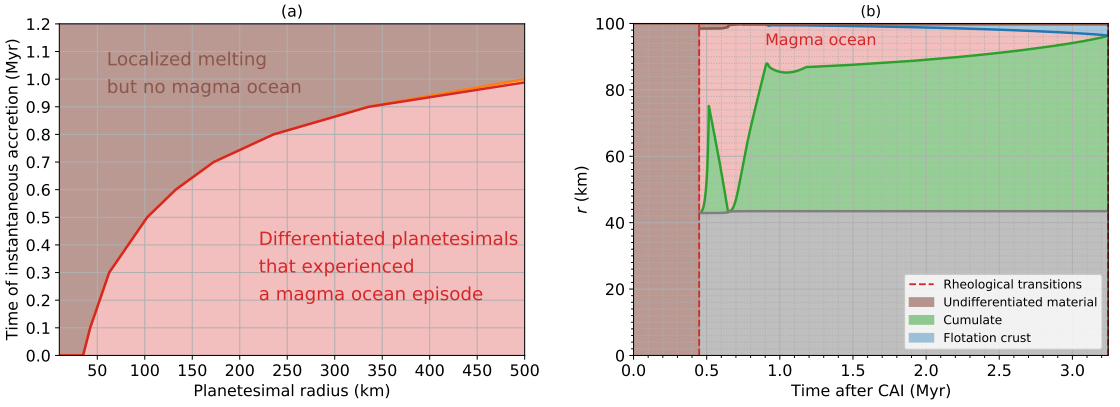

Figure 4: Instantaneous accretion. (a): Diagram showing the conditions (radius R and accretion time t_0) of for a planetesimal to differentiate. (b): Evolution of the internal structure evolution of a 100 km radius planetesimal that accreted instantaneously at $t_0 = 0$ Myr.

3.2. Structure evolution during planetesimals accretion

To illustrate the typical thermal history of an accreting planetesimal that undergoes a magma ocean episode, we consider a parent body with a final radius $R_f = 100$ km. To start with, we consider the following parameters of the accretion law, consistent with the "protracted accretion" domain: $R_0/R_f = 0.5$, $t_{acc} = 0.4$ Myr and $\beta = 0.5$. The time evolution of the internal structure, the surface heat flux, the bulk temperature, and the Shields number are shown in Figure 5. During the first 0.7 Myr, heat is dissipated by conduction only. At 0.7 Myr the rheological transition is reached and instantaneous and complete core-mantle differentiation occurs thanks to the low viscosity of the medium. Only a relatively thin crust, relic of the stagnant lid, remains at the surface. As chondritic material keeps being accreted, the thickness of this crust grows, with an increasing insulating effect on the magma ocean. Consequently, the bulk magma ocean temperature becomes larger than the silicate rheological transition temperature which induces the basal melting and iron segregation from the lower crust. Note that this increasing temperature episode also produces the melting to some extent of the first deposited cumulate. As the melting of the chondritic material proceeds, its iron component is incorporated into the core. Protracted accretion keeps bringing new material that globally thickens the crust and contributes to its insulation effect. As ^{26}Al is still active, albeit with a decreasing power, the crust continues to melt and to segregate iron at its base. This feedback effect causes successive melting episodes spanning from 0.7 to 2.3 Myr with several local maxima visible both on the heat flux and bulk temperature. The magma ocean temperature is buffered just above the rheological transition temperature after the first maximum. The value of this absolute maximum can be as high as the silicate liquidus temperature, provided the planetesimal terminal radius is large enough (see Appendix C). After 2.3 Myr, ^{26}Al source has been largely exhausted, and there is no more crust melting. At high temperatures only heavy crystals are formed and sediment, but magma ocean continuous cooling starts to produce light crystals forming a flotation crust beneath the chondritic crust. The rheological transition is reached in the bulk of the silicate mantle at 4 Myr, and the magma ocean freezes. At this point the convection regime transitions back to solid-state convection.

Two key elements should be emphasized in this scenario. First, as the protracted accretion occurs on a longer timescale than the half-life of the radioactive elements, the primordial heat released in the magma ocean is moderate enough to enable the preservation of a km size crust even early in the thermal history. Second, internal heat production induces crustal melting episodes over a few Myr period. The intensity of these phenomena is a function of the amount of primordial heat stored in the magma ocean, and, correspondingly, by the size of the planetesimal. In the following, we discuss how this kind of model can be used to interpret meteoritical data, taking EC002 as an example.

3.3. Lower bound of parent body size: important partial melting episodes in the lower crust

The first constraint we consider deals with the genesis of the parent magma. EC002 is though to have been formed by 25% partial melting of chondritic material that constitutes the early crust of the parent body. We have found in our model (i) that this type of crust is likely to exist, (ii) that partial melting of the lower part of the crust is usual. To obtain more detailed information on EC002 parent body, we can evaluate the time at which the crustal melting episode occurs as a function of the planetesimal size. Results are displayed in Figure 6 (a). In the case of protracted accretion,

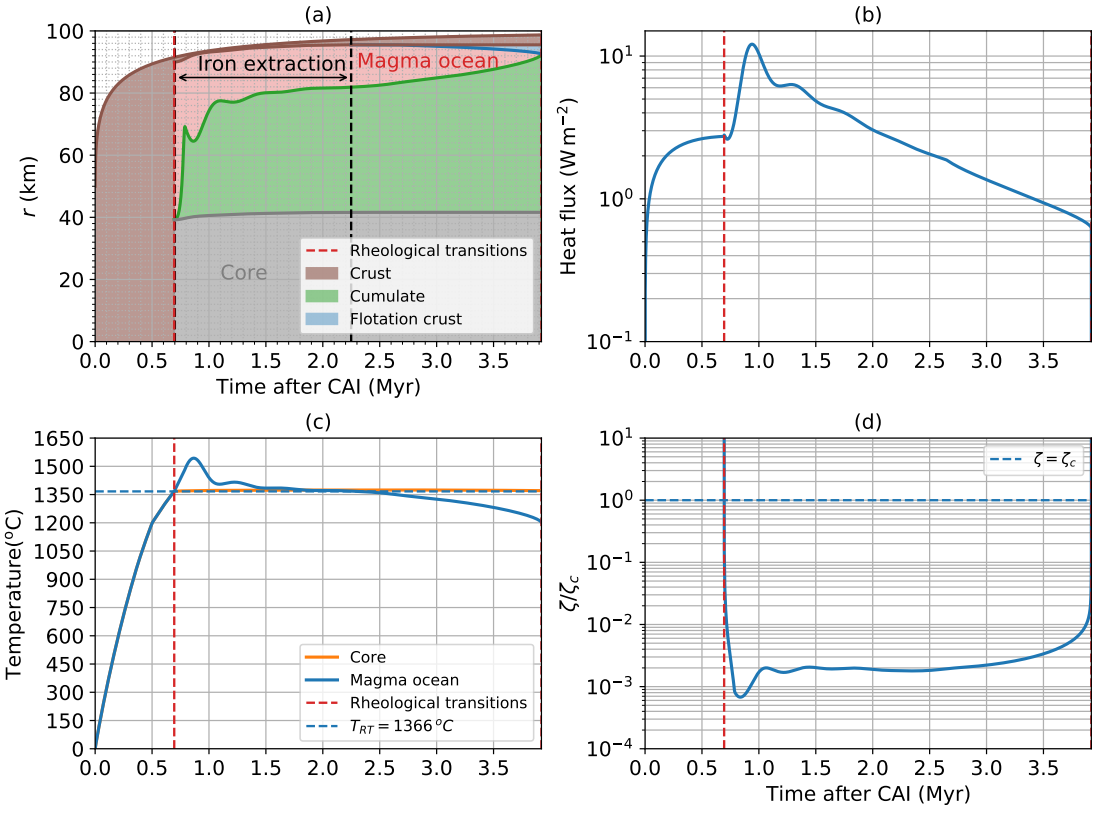

Figure 5: Typical evolution of a 100 km terminal radius planetesimal that begins its protracted accretion at $t = 0$ Myr ($R_0/R_f = 0.5$, $t_{acc} = 0.4$ Myr, $\beta = 0.5$). (a): Evolution of the internal structure of the accreting planetesimal. Magma ocean episode begins at the rheological transition (red vertical dashed line), and yields core/mantle differentiation. The crust is stable and thickens due to accretion supply. Insulation effect of the crust leads to iron extraction at its base between 0.7 to 2.3 Myr. When magma ocean temperature is sub-liquidus, crystals nucleate and deposits form, first a cumulate at CMB, then a floating deposit. Note that the early formed cumulate remelts partially during the crustal thinning episode. We also display the surface heat flux (b), the temperature of the magma ocean and the core (c) and the evolution of the Shields number in the magma ocean (d) during the planetesimal evolution.

a magma ocean episode occurs in planetesimals with final radius $R_f > 55$ km. The larger the planetesimal, the earlier the melting begins and the longer this magma ocean episode lasts. This can be explained by the ratio between the surface heat losses over the heat generated by the radioactive source that scales with the surface over volume ratio, and decreases with the planetesimal size. Consequently, the larger the planetesimal, the more heat from radioactive decay is stored.

We assume that the parent magma of EC002 has been formed during this massive partial melting episode of the crust. As a consequence, the melting period has to encompass the date derived from geochronology. According to Figure 6 (a), we deduce that the planetesimal final radius has to be larger than 80 km in order to undergo a crustal melting episode consistent with the time at which EC002 parent magma was produced ($\approx$ 1.8 Myr).

3.4. Upper bound of the parent body size: EC002 has to be preserved in a "chondritic fridge"

A cooling rate of 5 °C yr^{-1} has been inferred for EC002 from petrological data. Such a rate is consistent with the thermal evolution of a few tens of meters size magmatic reservoirs buried about 1 km below the surface – see Appendix B. The depth of storage of the magma corresponds to its neutral buoyancy relative to the crustal material. In the shallowest layers of the planetesimal crust, the density is mainly controlled by the porosity, which itself results from the brecciation induced by the impacts. It is thus likely that the magma reservoirs form at the base of the regolith.

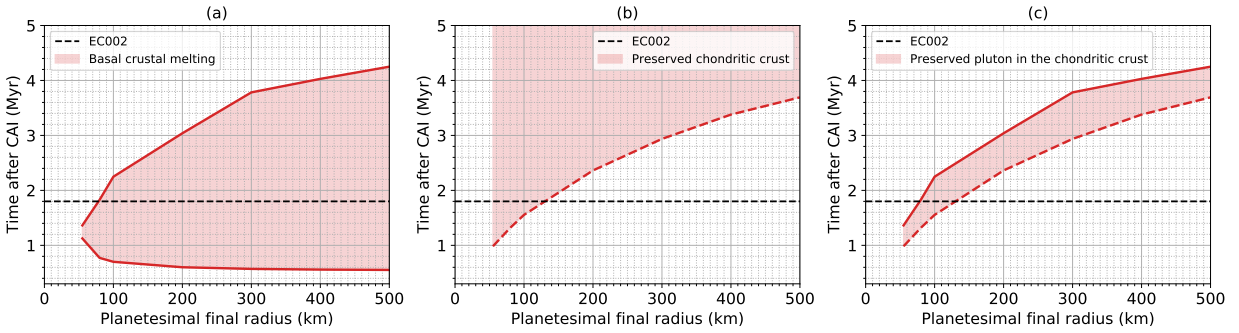

Figure 6: (a) Duration of the crustal melting episode in accreting planetesimal as a function of the planetesimal final radius. (b) Time t_{CF} at which the chondritic material supplied by accretion is preserved as a undifferentiated crust as a function of the planetesimal final radius. (c) Abacus showing the time at which the magma stored in the chondritic crust is preserved as a function of the planetesimal final radius. All simulations are performed with $\beta = 0.5$, $t_{acc} = 0.4\,\mathrm{Myr}$ and $R_0/R_f = 0.5$. In the three sub-panels, the horizontal line gives the time at which the parent magma of EC002 rises in the crust according to petrological data ($\approx 1.8\,\mathrm{Myr}$).

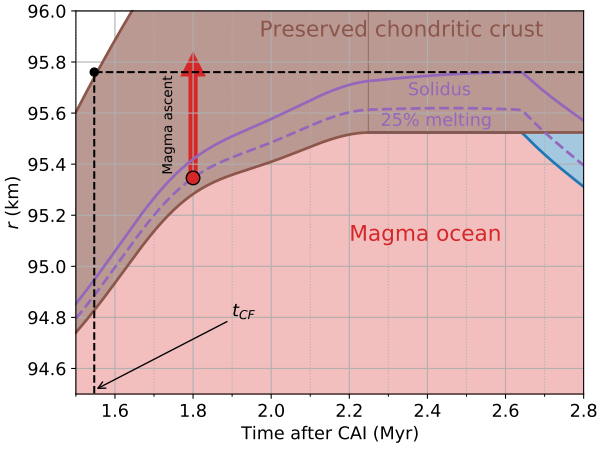

Figure 7: Zoom on the upper layers of the planetesimal showing constraints on the time at which a magma produced by 25% of melting in the chondritic crust and that has risen into the crust (dashed purple line) can be preserved form subsequent remelting. Only magma produced after t_{CF} can be preserved from remelting (i.e. their temperature remains below the solidus, solid dashed line). Here, we use the following parameters: $R_f = 100$ km, $R_0/R_f = 0.5$, $t_{acc} = 0.4$ Myr, $\beta = 0.5$.

The scenario that models the evolution of the parent magma of EC002 is displayed in Figure 7. The magma parent forms by 25% partial melting of chondritic material. At 1.8 Myr, the magma is stored at the base of the regolith, at a depth where it must be preserved from remelting (horizontal dashed line in Figure 7). We assume that this transfer happened by melt channeling hence is quasi instantaneous (Spiegelman, Kelemen and Aharonov, 2001; Chauveau and Kaminski, 2008). The depth at which the pluton is preserved from remelting is materialized by the horizontal dashed line in Figure 7. This depth can be translated into a corresponding time t_{CF} at which the chondritic material supplied by accretion is preserved as an undifferentiated crust (t_{CF} = "chondritic fridge" time). Figure 6 (b) displays this time as a function of the planetesimal final radius.

We combine the two constraints (magma ascent occurring during a crustal melting episode, and no subsequent re-melting) to build an abacus relating the size of the parent body to the time at which the magma crystallizes (Figure 6 (c)). This abacus gives the size of the parent body of a meteorite as a function of the date at which the parent magma crystallizes. For instance, for a crystallization time of 1.8 Myr, as it seems to be the case for EC002, the parent bodies should have had a final radius between 80 and 130 km.

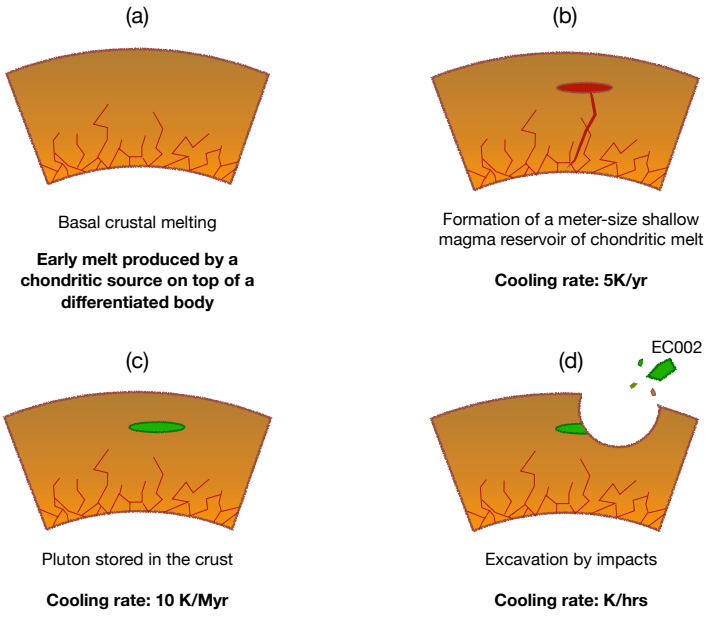

Figure 8: Proposed genesis and thermal history of EC002. (a) Partial melting of the chondritic lower crust generates the parent magma. (b) Magma rises to a shallow storage depth. (c) The parent magma crystallizes quickly and forms a pluton. (d) The pluton is excavated by an impact. Note that the crust thickens continuously during the thermal history, due to accretion of cold material. For sake of simplicity, this figure does not show this effect.

The thermal equilibration of the so-formed pluton is quasi-instantaneous (≈ 40 yr) compared to the characteristic timescale of crustal thermal evolution (several Myr). Then, the magma evolves as a pluton stored in the crust where it further cools down at a rate of a few ^{o}C Myr^{-1}. Barrat et al. (2021) proposed that EC002 further experienced a high cooling rate of $0.1 - 1^{o}$C/day when it had cooled down below a temperature of 900^{o}C, which would be consistent with cooling subsequent to an excavation by impact. The genesis and the complete thermal history of EC002 can then be summarized schematically in Figure 8.

3.5. Sensitivity to the accretion law parameters

In the previous section we estimated the final radius of the parent body of EC002 between 80 and 130 km, and we obtained that its chondritic crust was a few km thick. To obtain these results we used a protracted accretion law based on three parameters (R_0/R_f, $t_{\rm acc}$ and β) that presumably influence the thermal evolution of the planetesimal. We already highlighted that for R_0/R_f ranging from 0 to 0.8, the accretion history remains largely unchanged. As a consequence, our results are not affected by R_0/R_f within this range. Parameters β and t_{acc} induce a characteristic timescale for accretion $\tau_{99\%}$ that (i) has to be consistent with the duration of the dissipation of the protoplanetary disk, (ii) must be greater that the decay of ^{26}Al. In the following, we explore the sensitivity of β in the range 0.5 and 1.5 for $t_{acc} = 0.4$ Myr, and we test t_{acc} from 0.07 Myr to 0.87 Myr with $\beta = 0.5$.

3.5.1. Influence of β

We first consider the influence of β on the onset of the magma ocean episode and of the crustal melting. We fix the parameters $R_0/R_f = 0.5$ and $t_{acc} = 0.4$ Myr and we present results for three values of β (0.38, 0.5, 1.5 Myr), resulting from the intersection with the limits of the "protracted accretion" domain in Figure 2(b). Figure 9 shows that the magma ocean characteristics depends only slightly on β. Planetesimals with final radius $R_f > 55$ km trigger a magma ocean with an onset time always ranging from 0.5 to 1.5 Myr. The duration of the magma ocean is also robust, spanning over 2 to 10 Myr. The episode of crustal thinning and melting depends on β. The larger the value of β, the shorter the duration of crust melting.

Figure 10 (a) contains the abacus showing the time at which magma stored in the chondritic crust is preserved for the three values of β. For relatively small values of β, that correspond to high values of $\tau_{99\%}$, the two zones are

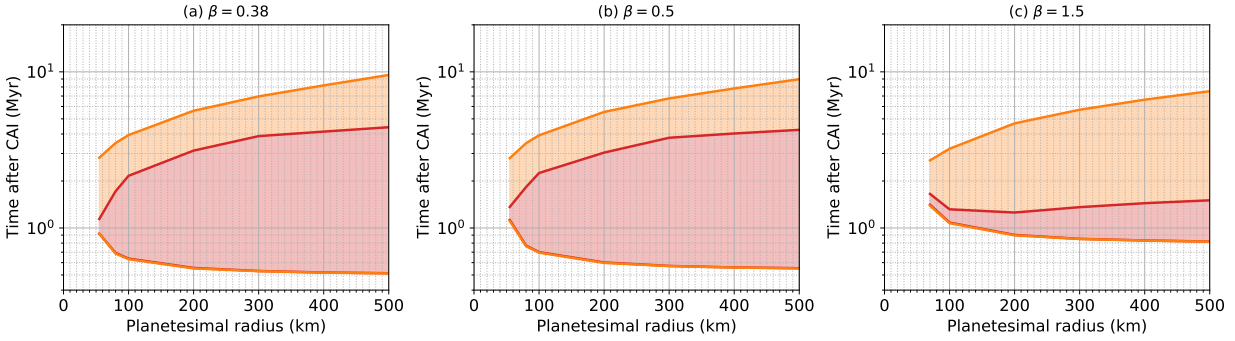

Figure 9: Influence of β on the lifetime of the magma ocean (orange) and on the onset and duration of the crustal melting event (red) for planetesimals with terminal radius spanning from 40 to 500 km and $t_{acc} = 0.4\,\mathrm{Myr}$.

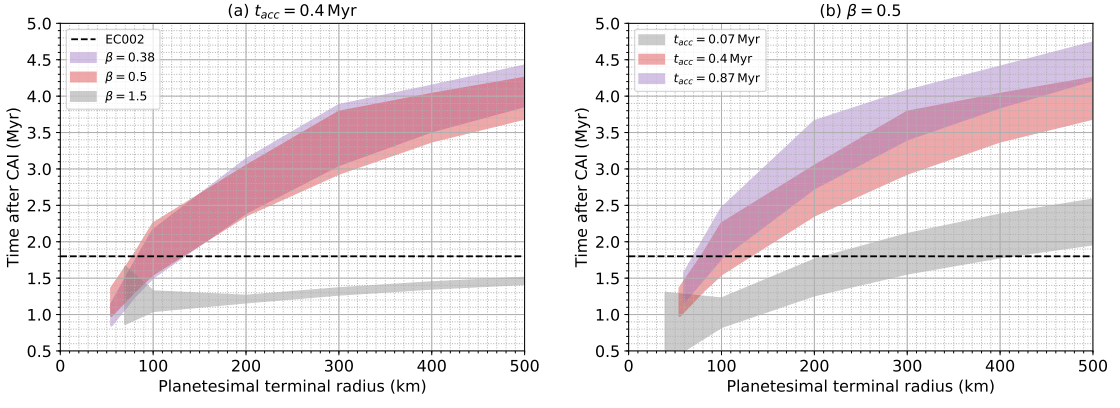

Figure 10: Abacus showing the parent body size required to produce 25% partial melting in the lower crust and later preservation of the produced differentiated rock once it has been stored in the shallow crust. These abacuses are made following the sensitivity study described in the text. (a) Influence of β. (b) Influence of t_{acc}. The horizontal black dashed line gives the age inferred from EC002 (1.8 Myr). The color of the domains are set by the value of $\tau_{99\%}$: purple (10Myr), red (5Myr) and grey (1Myr).

almost identical. In this case the accretion is much slower than the decay of radioactive elements and consequently, after the first crustal melting episode, the chondritic crust is thicken by accretion, reaching a few km thick chondritic crust (see figure 11 (a), purple and red curves), which will restore the insulation of the magma ocean. Consequently, heat released by radioactivity is not efficiently evacuated and the magma ocean temperature rises, along with the lower crust temperature, which, in turn, is able to produce partial melting of the crust. This induces cycles of crustal thinning and chondritic crust growing, which lengthens the episode of crustal melting. High values of β corresponds to quasi-instantaneous accretion (grey zone in Figure 10(a)). In this case, when the crust is thinned by basal melting and iron segregation, accretion is nearly finished, and thus the crust cannot grow though the external supply of chondritic material, and less than 1 km crust remains at the end of the accretion (see also figure 11 (a), grey curve). In this case, the first crustal thinning and melting episode increases the heat losses, which rapidly balances the heat released by radioactive elements.

We conclude that β is an important parameter for the history of the accreting planetesimal. Smaller values of β correspond to parent bodies with a thicker "chondritic fridge" (a few km). The crust melting episode spans the time range between 1 and 4 Myr. EC002 data are therefore consistent with this family of planetesimals. Higher values of β correspond to planetesimals that are unable to preserve a substantial undifferentiated crust, as undifferentiated material is brought early compared to the decay of radioactive elements (in other words they have a small $\tau_{99\%}$).

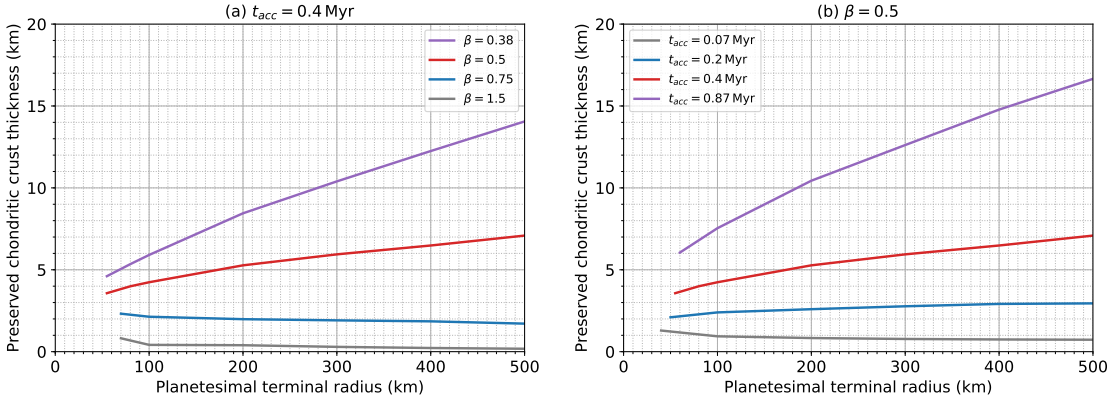

Figure 11: Thickness of the chondritic crust as a function of planetesimal final radius for different values of β (a) with t_{acc} = 0.4 Myr and of t_{acc} (b) with $\beta = 0.5$. $R_0/R_f = 0.5$. The color of the curves are set by the value of $\tau_{99\%}$: purple (10Myr), red (5Myr), blue (2Myr), grey (1Myr).

3.5.2. Influence of t_{acc}

We also evaluate the influence of t_{acc} on the size of EC002 parent body (Figure 10 (b)). The red zones in Figures 10(a) and (b) are identical and correspond to the values of parameters $\beta = 0.5$ and $t_{acc} = 0.4$ Myr, represented by the red star in Figure 2 (b). We take the two end-members for $\beta = 0.5$ corresponding to the intersection with the limits of the "protracted accretion" domain in Figure 2 (b): t_{acc} ranges from 0.07 to 0.87 Myr. Small values of t_{acc} correspond to an accretion history that is close to an instantaneous one, whereas high values of t_{acc} correspond to a longer accretion timescale. The parent body of EC002 should have a final radius R_f in the range from 70 to 100 km for $t_{\rm acc} = 0.87$ Myr, from 80 to 130 km for $t_{\rm acc} = 0.4$ Myr and from 210 to 400 km for $t_{acc} = 0.07$ Myr (Figure 10 (b)). The thickness of the preserved chondritic crust increases with t_{acc}, and small values of t_{acc} are not consistent with the preservation of a pluton in an undifferentiated crust (crust thickness < 1km), and hence, cannot explain EC002 formation (Figure 11(b), grey curve). Figure 11 also displays two curves that correspond to values of β and τ_{acc} from the intersection with $\tau_{99\%}$=2Myr (blue curves). They indicate that a substantial crust, of 2-3 km, can be produced and later preserved only for larger values of $\tau_{99\%}$. Figures 10 and 11 point out that apparently the most important parameter for the accretion history is $\tau_{99\%}$, and not the individual β and τ_{acc} producing it.

Based on this sensitivity study, the parent body of EC002 radius can be estimated thanks to the Figure 10. If we exclude cases lying too close to the "quasi instantaneous accretion", the parent body of EC002 has a final radius R_f between 70 and 130 km. We highlighted that the characteristics of the preserved chondritic crust and the thermal history are linked to the comparison between the characteristic accretion timescale $\tau_{99\%}$ and the half-life of ^{26}Al ($t^{Al}_{1/2}$ =0.717 Myr), which should be a factor of about 3 times larger ($\tau_{99\%} > 2$Myr).

The onset time of crustal melting and the "chondritic fridge" time t_{CF} are the two conditions that set bounds to the accretion history of a planetesimal consistent with EC002. They both should be lower than the crystallization time measured for EC002 (1.8 Myr); the first condition ensures the existence of the parent magma and the second one the preservation of the pluton in the crust. These conditions limit the parameters of the accretion law to the shaded zone in Figure 12.

4. Other geophysical implications

4.1. Sustainable "chondritic fridge" at the surface of planetesimals

Our model, applied in the previous section to the thermal history of EC002, actually describes general features in the evolution of planetesimals. In particular, considering a protracted accretion has an important impact on the planetesimal structure. Early instantaneous accretion induces very intense internal heating, due to the large amount of ^{26}Al that is stored. As a consequence, the peak bulk temperature is so high that any crust present at the surface is bound to melt and to become very thin (below 1 km). Protracted accretion will balance internal heating by the addition of cold material and will thus help to preserve a relatively thick crust that may later undergo melting episodes (Figure

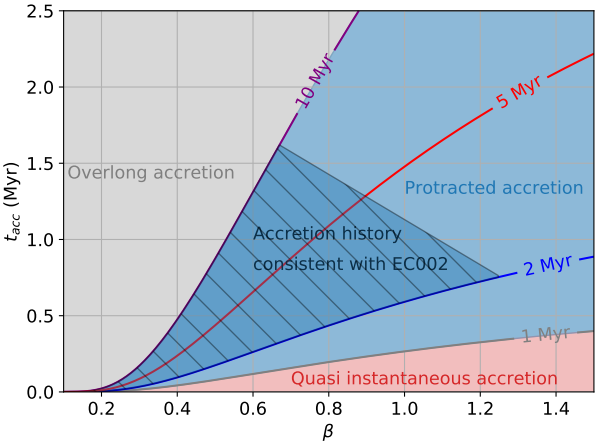

Figure 12: Parameters of the accretion law consistent with EC002.

11). These phenomena favor the formation of evolved rocks in planetesimals that preserve information from the early times of their history. For instance, some meteorites bear traces of early dynamos on their parent bodies, as the Kaba meteorite that recorded a dynamo as early as 10 Myr after CAI (Gattacceca, Weiss and Gounelle, 2016). Dodds et al. (2021) calculated that planetesimal cores with radius larger than 400 km (i.e., planetesimals with radius higher than $\approx$ 918 km) are able to sustain a dynamo at these early times. But the crust in the case of instantaneous accretion remains only $\approx$ 1 km thick so that it is unlikely it could register a remanent magnetization. To avoid crustal melting, the authors made the accretion begin at 0.8 Myr after CAIs, which corresponds roughly to a decay of ^{26}Al to half of its initial value. In the case of a protracted accretion that begins at $t = 0$ and a planetesimal with $R_f = 920$ km, our model predicts at 10 Myr a 49 km thick crust including (i) a 15 km thick chondritic upper crust, (ii) a 1 km thick layer and (iii) a 33 km thick differentiated layer of floating crystals. The undifferentiated part of the crust lies below the Curie temperature ($\approx 800^{o}$C) which would provide suitable conditions for the record of the early magnetic activity. This cold zone is a natural consequence of protracted accretion, in contrast with the runaway accretion scenario used by Dodds et al. (2021) in which accretion ends early. A more detailed modeling of the possibility to sustain a dynamo in this type of body is required (Monteux, Jellinek and Johnson, 2011; Bryson et al., 2019; Dodds et al., 2021) in order to provide a precise information on the time at which the dynamo is triggered.

4.2. Geochronology of iron meteorites

The Hf $-$ W systematics established for iron meteorites bring some constraints to refine their accretion scenario. Hf $-$ W age is usually interpreted as the date of instantaneous core formation (Kruijer et al., 2014). However, if the contribution of iron from crustal melting occurs over a long period of time, ages inferred from Hf $-$ W systematics integrate the entire process of differentiation (Neumann, Kruijer, Breuer and Kleine, 2018). We calculated the proportion of the core that is supplied by core melting (Figure 13 (a)) and the apparent age of the core inferred from Hf $-$ W systematics using our model, and we display it as a function of the time of the first differentiation in Figure 13 (b). In order to illustrate this effect we show in these figures only the results obtained for accretion histories characterized by $\tau_{99\%}$=5 Myr (red curves) or $\tau_{99\%}$=10 Myr (purple curves). The proportion of core added during accretion and crust melting is less important for lower values of the accretion timescale $\tau_{99\%}$ (data not shown). Within the displayed values (Figure 13 (a)) the volume of core added depends on the values of the group of parameters (β and τ_{acc}), the larger they are, the bigger the effect. The first differentiation occurs at the rheological transition that happens at 0.5 $-$ 1.5 Myr, while the apparent age of the core is always younger than the age of the first differentiation, and can be very different, depending on the values of the accretion parameters we are ready to admit. There is also a dependence of the volume of core added with the final planetesimal radius R_f which reaches a plateau at large values. The apparent age of the core does not reach a similar plateau and actually continues to strongly increase with R_f.

These considerations can be used to interpret the age dichotomy in the iron meteorites. Earlier Hf $-$ W inferred ages range from 0.5 to 1.5 Myr for non-carbonaceous (NC) magmatic iron meteorites, and from 2 to 3 Myr for carbonaceous (CC) magmatic iron meteorites (Kruijer et al., 2014, 2017). Recent revised Hf $-$ W model ages corrected

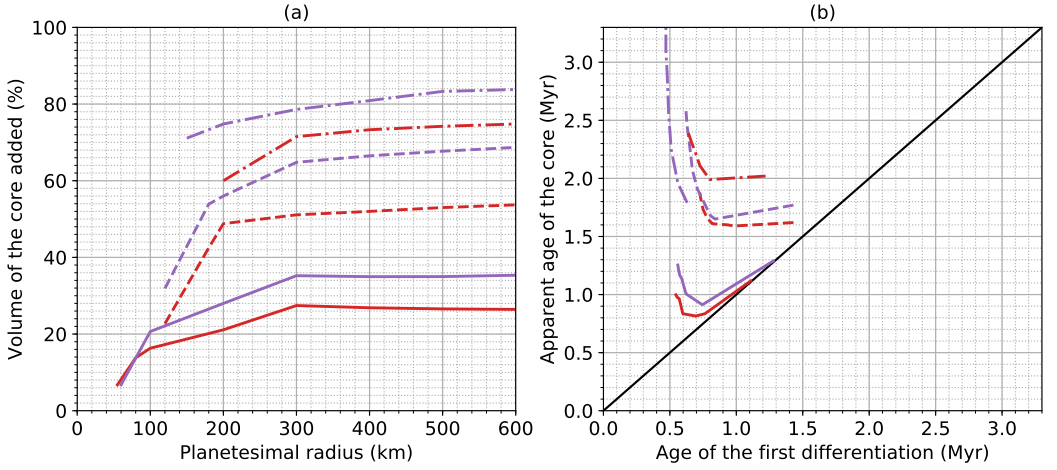

Figure 13: (a) Proportion of the core that is brought by iron supply due to progressive melting of the chondritic crust as a function of the planetesimals final radius. (b) Apparent age of the core inferred from Hf − W systematics as a function of the age of the first differentiation that corresponds to the onset of the magma ocean. Black line represent a 1:1 dependence between the two ages. Red curves represent values of $\tau_{99\%}$ =5 Myr and purple curves $\tau_{99\%}$ =10 Myr, full lines β=0.5, dashed lines β=1 and dashed and dotted lines β=1.5.

for nucleosynthetic Pt isotope variations are slightly younger ($1-2$ Myr for NC meteorites and $3-3.5$ Myr for CC meteorites (Spitzer, Burkhardt, Nimmo and Kleine, 2021)). In the case of NC iron meteorites, these younger ages were confirmed by Mn − Cr chronometry ($0.4-2.2$ Myr) (Anand, Pape, Wille, Mezger and Hofmann, 2021).

Our model can explain the entire age range estimated for NC iron meteorites, for accretion histories characterized by values of (β and τ_{acc}) rather small, and small to intermediate values of the final planetesimal radius R_f. Ages of CC iron meteorites can be obtained for large values of R_f and large values of the pair of parameters (β and τ_{acc}) that result in large values of $\tau_{99\%}$ falling between the red (5 Myr) and purple (10 Myr) lines in Figure 2.

Although we can explain the age range encompassed by both NC and CC iron meteorites, we nevertheless acknowledge that thermal modeling of CC bodies requires a specific study. The substantial presence of water and other volatiles modifies almost everything in the model, from the heat budget by the intermediate of the latent heat to other properties susceptible to affect convection such as the viscosity. The present model with the values of parameters in Table 1, properly describes only the formation of dry, NC bodies.

4.3. Degassing despite a "chondritic fridge"?

The presence of a "chondritic fridge" on top of planetesimals rises the question of volatile behavior in such systems. The surface temperature is taken as a constant, which is a reasonably good approximation (less than 10 K variation) for small radius planetesimals heated by ^{26}Al (Dodds et al., 2021). More rigorously, the surface temperature results from the balance between the emitted radiative flux, the absorbed solar radiative flux and the heat flux at the surface of the body (Henke, Gail, Trieloff and Schwarz, 2013). The (quasi)isothermal boundary condition and low temperature at the surface will determine the preservation of a stagnant lid. A planetary body with a sub-surface magma ocean can be subject to partial or total crust melting and therefore go through volatile loss and EC002 meteorite can be taken as a proof of such magmatic activity. The amplitude and timescale of this magmatic activity should depend mainly on the body radius and the distance to the sun. We cannot rule out a transitory disruption of the crust during the first few Myr. A transitory disruption of the stagnant lid and the exposure of molten rock at the surface would lead to a transitory increase of the radiative heat flux which will cool down the surface and restore the isothermal boundary condition with the aid of the newly accreted, cold material. This transitory episode should be very short with respect to the duration of the magma ocean, provided planetesimals cannot preserve an atmosphere. This should be the case for the small radius bodies like the ones considered in the present study. Degassing is hence possible even though the planetesimal is covered by a "chondritic fridge" as established in a large number of studies (Norris and Wood, 2017;

Young, Shahar, Nimmo, Schlichting, Schauble, Tang and Labidi, 2019; Sossi, Klemme, O'Neill, Berndt and Moynier, 2019; Collinet and Grove, 2020; Hirschmann, Bergin, Blake, Ciesla and Li, 2021).

5. Conclusion

We highlighted in this paper how geochemical and petrological data obtained from differentiated achondrites can be used to constrain the formation and evolution of their parent bodies. Our results are based on a thermal model that takes into account protracted accretion, core-mantle differentiation, magma ocean episode and crustal thickening by continuous accretion of chondritic material at the surface. This model predicts that the reference internal structure of a planetesimal formed early with a size $\gtrsim 55$ km is a differentiated interior (with a liquid metallic core and a crystallizing magma ocean) covered by an undifferentiated chondritic crust that is stable and will undergo localized basal partial melting. We show how cooling rates provide information about the depth and the size of the reservoir where the parent magma of achondrites crystallized in the chondritic crust. The datation of parent magma formation can then be used to provide some bounds on the parent body size and on the parameters of its accretion laws. This approach is general and could be used to study other parent bodies than that of EC002.

Acknowledgments

This paper is part of Cyril Sturtz's PhD thesis (Université Paris Cité, Institut de Physique du Globe de Paris). The authors would like to thank the editor Doris Breuer for her editorial handling and two anonymous reviewers for their fruitful comments that improve this manuscript. This study contributes to the IdEx Université de Paris ANR-18-IDEX-0001. This work was supported by the Programme National de Planétologie (PNP) of CNRS/INSU, co-funded by CNES.

A. Rheological law and composition as a function of the temperature

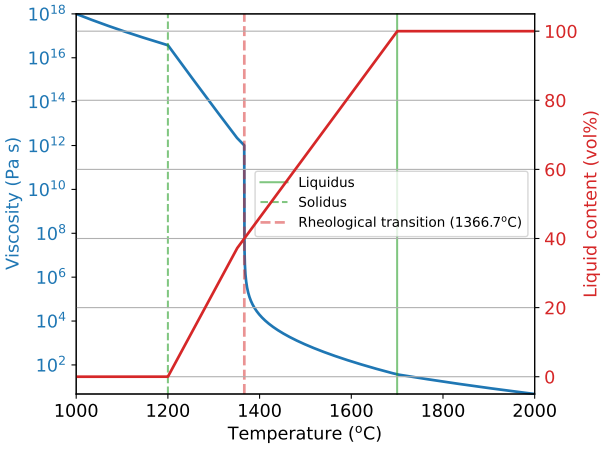

Figure 14: Rheological law (blue) of the planetesimal and liquid fraction (red) in the body as a function of the temperature. We assume an equilibrium melting, so that the liquid content is directly given by (4). The rheological transition occurs for a liquid content of 40% (i.e.: a solid content of 60%).

B. Cooling model for a magmatic reservoir buried at a certain depth

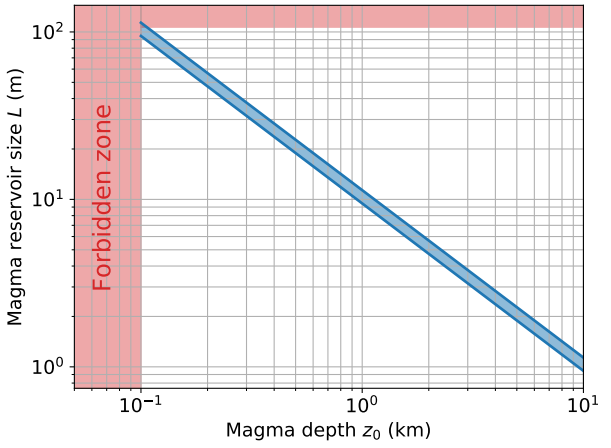

Figure 15: Evolution of the size of a magmatic reservoir that undergoes a cooling rate of 5 °C/yr as a function of the depth at which it is stored. The area colored in blue stands for temperature anomalies spanning from 1000 to 1200 °C. The forbidden zone represents non-physical solutions that implies reservoirs that are larger than the crust thickness.

The cooling rates measured in some crystals provide constraints on the condition of magma storage in the crust. For a cooling rate of $5\,^{\circ}\mathrm{C\,yr^{-1}}$, like the one measure in EC002, a simple model for the cooling of a magma reservoir can predict the size and the depth at which magma is stored. We consider a magma body of typical length L at a depth z_0 bearing a thermal anomaly ΔT compared to the surface temperature T_s. During a quasi-static evolution of a period of time dt, the variation of internal energy is $\rho c_p \mathrm{d}(\Delta \mathrm{T})\,\mathrm{LS}$, where S is the surface of the system through which heat losses occur. The heat flux can be written $Q_s\,S\,\mathrm{dt}$, where Q_s is assumed to be conductive (Kaminski and Jaupart, 2000)

and the conservation of energy yields

$$\frac{\mathrm{d}\Delta \mathrm{T}}{\mathrm{dt}} = \frac{\lambda}{\rho c_p} \frac{\Delta T}{z_0 L}, \tag{40}$$

where λ is the thermal conductivity of the enclosing rock, ρ is its density and c_p its specific heat. Results of magma reservoir size as a function of its depth to get the required cooling rate are displayed in Figure 15. To attain $5\,^{\circ}\mathrm{C\,yr^{-1}}$, the magma has to be stored in small reservoir, which means that the reservoir that cools is a few meter size diapir or a magma lens stored at a few km depth.

Furthermore, this approach shows that the shallower the reservoir the larger its size for a given cooling rate. This calculation predicts also that the crust of the parent body has to be thicker than 100 m in order to sustain a reservoir whose size is smaller than the crust thickness and at least 300 m in order to have reservoirs that represents 10% of the crust thickness (Figure 15).

C. Maximum temperature reached in the magma ocean

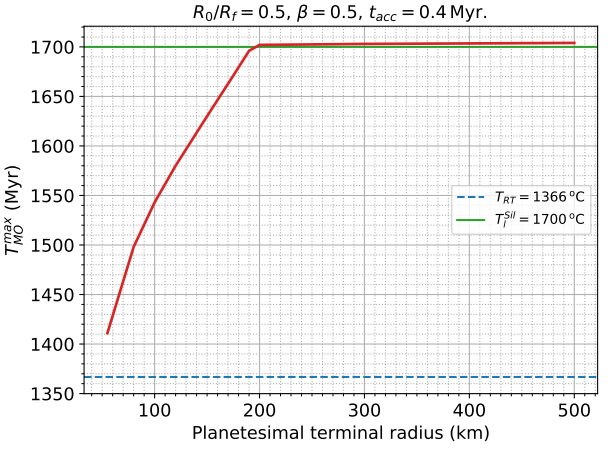

Figure 16: Maximum temperature reached during the crust melting and iron extraction episode as a function of the terminal planetesimal radius R_f.

References

Agee, C., Habermann, M., Ziegler, K., 2018. Northwest africa 11575: Unique ungrouped trachyandesite achondrite, in: Lunar and Planetary Science Conference, p. 2226.

Allègre, C., Manhès, G., Göpel, C., 1995. The age of the earth. Geochimica et Cosmochimica Acta 59, 1445–1456. URL: https://www.sciencedirect.com/science/article/pii/0016703795000544, doi:https://doi.org/10.1016/0016-7037(95)00054-4.

Anand, A., Pape, J., Wille, M., Mezger, K., Hofmann, B., 2021. Early differentiation of magmatic iron meteorite parent bodies from mn–cr chronometry. Geochemical Perspectives Letters 20.

Barrat, J.A., Chaussidon, M., Yamaguchi, A., Beck, P., Villeneuve, J., Byrne, D.J., Broadley, M.W., Marty, B., 2021. A 4,565-my-old andesite from an extinct chondritic protoplanet. Proceedings of the National Academy of Sciences 118. URL: https://www.pnas.org/content/118/11/e2026129118, doi:10.1073/pnas.2026129118, arXiv:https://www.pnas.org/content/118/11/e2026129118.full.pdf.

Bischoff, A., Horstmann, M., Barrat, J.A., Chaussidon, M., Pack, A., Herwartz, D., Ward, D., Vollmer, C., Decker, S., 2014. Trachyandesitic volcanism in the early solar system. Proceedings of the National Academy of Sciences 111, 12689–12692. URL: https://www.pnas.org/content/111/35/12689, doi:10.1073/pnas.1404799111, arXiv:https://www.pnas.org/content/111/35/12689.full.pdf.

Bouvier, A., Wadhwa, M., 2010. The age of the solar system redefined by the oldest pb–pb age of a meteoritic inclusion. Nature Geoscience 3, 637–641. URL: https://doi.org/10.1038/ngeo941, doi:10.1038/ngeo941.

Bryson, J.F., Neufeld, J.A., Nimmo, F., 2019. Constraints on asteroid magnetic field evolution and the radii of meteorite parent bodies from thermal modeling. Earth and Planetary Science Letters 521, 68–78. URL: https://www.sciencedirect.com/science/article/pii/S0012821X19303280, doi:https://doi.org/10.1016/j.epsl.2019.05.046.

Carslaw, H.S., Jaeger, J.C., 1959. Conduction of heat in solids. Oxford University Press, New York.

Charru, F., Mouilleron, H., Eiff, O., 2004. Erosion and deposition of particles on a bed sheared by a viscous flow. Journal of Fluid Mechanics 519, 55–80. doi:10.1017/S0022112004001028.

Chauveau, B., Kaminski, E., 2008. Porous compaction in transient creep regime and implications for melt, petroleum, and co2 circulation. Journal of Geophysical Research: Solid Earth 113. URL: https://agupubs.onlinelibrary.wiley.com/doi/abs/10.1029/2007JB005088, doi:https://doi.org/10.1029/2007JB005088, arXiv:https://agupubs.onlinelibrary.wiley.com/doi/pdf/10.1029/2007JB005088.

Choblet, G., Sotin, C., 2000. 3d thermal convection with variable viscosity: can transient cooling be described by a quasi-static scaling law? Physics of the Earth and Planetary Interiors 119, 321–336.

Collinet, M., Grove, T.L., 2020. Widespread production of silica- and alkali-rich melts at the onset of planetesimal melting. Geochimica et Cosmochimica Acta 277, 334–357. URL: https://www.sciencedirect.com/science/article/pii/S0016703720301666, doi:https://doi.org/10.1016/j.gca.2020.03.005.

Condie, K.C., 2016. Chapter 10 - comparative planetary evolution, in: Condie, K.C. (Ed.), Earth as an Evolving Planetary System (Third Edition). third edition ed.. Academic Press, pp. 317–367. URL: https://www.sciencedirect.com/science/article/pii/B9780128036891000109, doi:https://doi.org/10.1016/B978-0-12-803689-1.00010-9.

Connelly, J.N., Bizzarro, M., Krot, A.N., Nordlund, Å., Wielandt, D., Ivanova, M.A., 2012. The absolute chronology and thermal processing of solids in the solar protoplanetary disk. Science 338, 651–655. URL: https://science.sciencemag.org/content/338/6107/651, doi:10.1126/science.1226919, arXiv:https://science.sciencemag.org/content/338/6107/651.full.pdf.

Cuzzi, J., Hogan, R., Shariff, K., 2008. Toward planetesimals: Dense chondrule clumps in the protoplanetary nebula. The Astrophysical Journal 687, 1432–1447. URL: https://doi.org/10.1086/591239, doi:10.1086/591239.

Davaille, A., Jaupart, C., 1993. Thermal convection in lava lakes. Geophysical Research Letters 20, 1827–1830. URL: https://agupubs.onlinelibrary.wiley.com/doi/abs/10.1029/93GL02008, doi:10.1029/93GL02008, arXiv:https://agupubs.onlinelibrary.wiley.com/doi/pdf/10.1029/93GL02008.

Day, J., Ash, R., Liu, Y., Bellucci, J., III, D., McDonough, W., Walker, R., Taylor, L., 2009. Early formation of evolved asteroidal crust. Nature 457, 179–182. URL: https://doi.org/10.1038/nature07651, doi:10.1038/nature07651.

Dodds, K.H., Bryson, J.F.J., Neufeld, J.A., Harrison, R.J., 2021. The thermal evolution of planetesimals during accretion and differentiation: Consequences for dynamo generation by thermally-driven convection. Journal of Geophysical Research: Planets 126, e2020JE006704. URL: https://agupubs.onlinelibrary.wiley.com/doi/abs/10.1029/2020JE006704, doi:https://doi.org/10.1029/2020JE006704, arXiv:https://agupubs.onlinelibrary.wiley.com/doi/pdf/10.1029/2020JE006704. e2020JE006704 2020JE006704.

Elkins-Tanton, L., 2012. Magma oceans in the inner solar system. Annual Review of Earth and Planetary Sciences 40, 113–139. URL: https://doi.org/10.1146/annurev-earth-042711-105503, doi:10.1146/annurev-earth-042711-105503, arXiv:https://doi.org/10.1146/annurev-earth-042711-105503.

Elkins-Tanton, L., Weiss, B., Zuber, M., 2011. Chondrites as samples of differentiated planetesimals. Earth and Planetary Science Letters 305, 1–10.

Fang, L., Frossard, P., Boyet, M., Bouvier, A., Barrat, J.A., Chaussidon, M., Moynier, F., 2022. Half-life and initial solar system abundance of 146sm determined from the oldest andesitic meteorite. Proceedings of the National Academy of Sciences 119, e2120933119.

Faure, F., 2020. Early silica crust formation in planetesimals by metastable silica-rich liquid immiscibility or cristobalite crystallisation: the possible origin of silica-rich chondrules. Scientific Reports 10, 4765. URL: https://doi.org/10.1038/s41598-020-61806-5, doi:10.1038/s41598-020-61806-5.

Fu, R.R., Elkins-Tanton, L.T., 2014. The fate of magmas in planetesimals and the retention of primitive chondritic crusts. Earth and Planetary Science Letters 390, 128–137. URL: https://www.sciencedirect.com/science/article/pii/S0012821X1400003X, doi:https://doi.org/10.1016/j.epsl.2013.12.047.

Ganino, C., Libourel, G., 2017. Reduced and unstratified crust in cv chondrite parent body. Nature Communications 8, 261. URL: https://doi.org/10.1038/s41467-017-00293-1, doi:10.1038/s41467-017-00293-1.

Gattacceca, J., Weiss, B.P., Gounelle, M., 2016. New constraints on the magnetic history of the cv parent body and the solar nebula from the kaba meteorite. Earth and Planetary Science Letters 455, 166–175. URL: https://www.sciencedirect.com/science/article/pii/S0012821X16304885, doi:https://doi.org/10.1016/j.epsl.2016.09.008.

Greenwood, R., Franchi, I., Jambon, A., Buchanan, P., 2005. Widespread magma oceans on asteroidal bodies in the early solar system. Nature 435, 916–918. doi:10.1038/nature03612.

Greenwood, R.C., Burbine, T.H., Franchi, I.A., 2020. Linking asteroids and meteorites to the primordial planetesimal population. Geochimica et Cosmochimica Acta 277, 377–406. URL: https://www.sciencedirect.com/science/article/pii/S0016703720301058, doi:https://doi.org/10.1016/j.gca.2020.02.004.

Guazzelli, E., Pouliquen, O., 2018. Rheology of dense granular suspensions. Journal of Fluid Mechanics 852. doi:10.1017/jfm.2018.548.

Haugbølle, T., Weber, P., Wielandt, D.P., Benítez-Llambay, P., Bizzarro, M., Gressel, O., Pessah, M.E., 2019. Probing the protosolar disk using dust filtering at gaps in the early solar system. The Astronomical Journal 158, 55.

Henke, S., Gail, H.P., Trieloff, M., Schwarz, W., 2013. Thermal evolution model for the h chondrite asteroid-instantaneous formation versus protracted accretion. Icarus 226, 212–228. URL: https://www.sciencedirect.com/science/article/pii/S0019103513002340, doi:https://doi.org/10.1016/j.icarus.2013.05.034.

Hevey, P., Sanders, I., 2006. A model for planetesimal meltdown by 26al and its implications for meteorite parent bodies. Meteoritics & Planetary Science 41, 95–106. URL: https://onlinelibrary.wiley.com/doi/abs/10.1111/j.1945-5100.2006.tb00195.x, doi:10.1111/j.1945-5100.2006.tb00195.x.

Hirschmann, M.M., Bergin, E.A., Blake, G.A., Ciesla, F.J., Li, J., 2021. Early volatile depletion on planetesimals inferred from c–s systematics of iron meteorite parent bodies. Proceedings of the National Academy of Sciences 118.

Höink, T., Schmalzl, J., Hansen, U., 2006. Dynamics of metal-silicate separation in a terrestrial magma ocean. Geochemistry, Geophysics, Geosystems 7. URL: https://agupubs.onlinelibrary.wiley.com/doi/abs/10.1029/2006GC001268, doi:10.1029/2006GC001268, arXiv:https://agupubs.onlinelibrary.wiley.com/doi/pdf/10.1029/2006GC001268.

Jaupart, C., Mareschal, J.C., 2010. Heat Generation and Transport in the Earth. Cambridge University Press. doi:10.1017/CBO9780511781773.

Johansen, A., Lambrechts, M., 2017. Forming planets vis pebble accretion. Annu. Rev. Earth Planet. Sci. 12451, 359–387.

Johansen, A., Oishi, J., Low, M.M.M., Klahr, H., Henning, T., Youdin, A., 2007. Rapid planetesimal formation in turbulent circumstellar disks. Nature 448, 1022–1025. URL: https://doi.org/10.1038/nature06086, doi:10.1038/nature06086.

Kaminski, E., Jaupart, C., 2000. Lithosphere structure beneath the phanerozoic intracratonic basins of north america. Earth and Planetary Science Letters 178, 139–149. URL: https://www.sciencedirect.com/science/article/pii/S0012821X00000674, doi:https://doi.org/10.1016/S0012-821X(00)00067-4.

Kaminski, E., Limare, A., Kenda, B., Chaussidon, M., 2020. Early accretion of planetesimals unraveled by the thermal evolution of parent bodies of magmatic iron meteorites. Earth and Planetary Science Letters 548, 116469. doi:https://doi.org/10.1016/j.epsl.2020.116469.

Karl E. Haisch, J., Lada, E.A., Lada, C.J., 2001. Disk frequencies and lifetimes in young clusters. The Astrophysical Journal 553, L153–L156. URL: https://doi.org/10.1086/320685, doi:10.1086/320685.

Kleine, T., Budde, G., Burkhardt, C., Kruijer, T.S., Worsham, E.A., Morbidelli, A., Nimmo, F., 2020. The non-carbonaceous–carbonaceous meteorite dichotomy. Space Science Reviews 216, 55. URL: https://doi.org/10.1007/s11214-020-00675-w, doi:10.1007/s11214-020-00675-w.

Krieger, I.M., Dougherty, T.J., 1959. A mechanism for non-newtonian flow in suspensions of rigid spheres. Transactions of the Society of Rheology 3, 137–152. URL: https://doi.org/10.1122/1.548848, doi:10.1122/1.548848.

Kruijer, T., Touboul, M., Fischer-Gödde, M., Bermingham, K., Walker, R., Kleine, T., 2014. Protracted core formation and rapid accretion of protoplanets. Science 344, 1150–1154.

Kruijer, T.S., Burkhardt, C., Budde, G., Kleine, T., 2017. Age of jupiter inferred from the distinct genetics and formation times of meteorites. Proceedings of the National Academy of Sciences 114, 6712–6716. URL: https://www.pnas.org/content/114/26/6712, doi:10.1073/pnas.1704461114, arXiv:https://www.pnas.org/content/114/26/6712.full.pdf.

Lavorel, G., Le Bars, M., 2009. Sedimentation of particles in a vigorously convecting fluid. Physical review. E, Statistical, nonlinear, and soft matter physics 80, 046324. doi:10.1103/PhysRevE.80.046324.

Li, R., Youdin, A.N., Simon, J.B., 2019. Demographics of planetesimals formed by the streaming instability. The Astrophysical Journal 885, 69.

Limare, A., Jaupart, C., Kaminski, E., Fourel, L., Farnetani, C., 2019. Convection in an internally heated stratified heterogeneous reservoir. Journal of Fluid Mechanics 870, 67–105. doi:10.1017/jfm.2019.243.

Limare, A., Kenda, B., Kaminski, E., Surducan, E., Surducan, V., Neamtu, C., 2021. Transient convection experiments in internally-heated systems. MethodsX 8, 101224. URL: https://www.sciencedirect.com/science/article/pii/S2215016121000170, doi:https://doi.org/10.1016/j.mex.2021.101224.

Mandler, B., Elkins-Tanton, L., 2013. The origin of eucrites, diogenites, and olivine diogenites: Magma ocean crystallization and shallow magma chamber processes on vesta. Meteoritics & Planetary Science 48, 2333–2349. URL: https://onlinelibrary.wiley.com/doi/abs/10.1111/maps.12135, doi:10.1111/maps.12135, arXiv:https://onlinelibrary.wiley.com/doi/pdf/10.1111/maps.12135.

Martin, D., Nokes, R., 1988. Crystal settling in a vigorously convecting magma chamber. Nature 332, 534–536. URL: https://doi.org/10.1038/332534a0, doi:10.1038/332534a0.

Martin, D., Nokes, R., 1989. A Fluid-Dynamical Study of Crystal Settling in Convecting Magmas. Journal of Petrology 30, 1471–1500. URL: https://doi.org/10.1093/petrology/30.6.1471, doi:10.1093/petrology/30.6.1471, arXiv:https://academic.oup.com/petrology/article-pdf/30/6/1471/4314225/30-6-1471.pdf.

Monteux, J., Jellinek, A., Johnson, C., 2011. Why might planets and moons have early dynamos? Earth and Planetary Science Letters 310, 349–359.

Morbidelli, A., Bottke, W., Nesvorný, D., Levison, H., 2009. Asteroids were born big. Icarus 204, 558–573. URL: https://www.sciencedirect.com/science/article/pii/S0019103509003029, doi:https://doi.org/10.1016/j.icarus.2009.07.011.

Morbidelli, A., Lambrechts, M., Jacobson, S., Bitsch, B., 2015. The great dichotomy of the solar system: Small terrestrial embryos and massive giant planet cores. Icarus 258, 418–429.

Neumann, W., Breuer, D., Spohn, T., 2012. Differentiation and core formation in accreting planetesimals. A&A 543, A141. URL: https://doi.org/10.1051/0004-6361/201219157, doi:10.1051/0004-6361/201219157.

Neumann, W., Breuer, D., Spohn, T., 2014. Differentiation of vesta: Implications for a shallow magma ocean. Earth and Planetary Science Letters 395, 267–280.

Neumann, W., Kruijer, T., Breuer, D., Kleine, T., 2018. Multistage core formation in planetesimals revealed by numerical modeling and hf-w chronometry of iron meteorites. Journal of Geophysical Research: Planets 123, 421–444.

Norris, C.A., Wood, B.J., 2017. Earth's volatile contents established by melting and vaporization. Nature 549, 507–510.

Righter, K., Drake, M., 1997. A magma ocean on vesta: Core formation and petrogenesis of eucrites and diogenites. Meteoritics & Planetary Science 32, 929 – 944. doi:10.1111/j.1945-5100.1997.tb01582.x.

Roberts, P., 1967. Convection in horizontal layers with internal heat generation. theory. Journal of Fluid Mechanics 30, 33–49. doi:10.1017/S0022112067001284.

Rubie, D., Melosh, H., Reid, J., Liebske, C., Righter, K., 2003. Mechanisms of metal-silicate equilibration in the terrestrial magma ocean. Earth and Planetary Science Letters 205, 239–255.

Sahijpal, S., Soni, P., Gupta, G., 2007. Numerical simulations of the differentiation of accreting planetesimals with 26al and 60fe as the heat sources. Meteoritics & Planetary Science 42, 1529–1548.

Schubert, G., Turcotte, D.L., Olson, P., 2001. Mantle convection in the Earth and planets. Cambridge University Press, Cambridge.

Scott, T., Kohlstedt, D.L., 2006. The effect of large melt fraction on the deformation behavior of peridotite. Earth Planet Sci. Lett. 216, 177–187.

Shearer, C., Burger, P., Neal, C., Sharp, Z., Spivak-Birndorf, L., Borg, L., Fernandes, V., Papike, J., Karner, J., Wadhwa, M., Gaffney, A., Shafer, J., Geissman, J., Atudorei, N.V., Herd, C., Weiss, B., King, P., Crowther, S., Gilmour, J., 2010. Non-basaltic asteroidal magmatism during the earliest stages of solar system evolution: A view from antarctic achondrites graves nunatak 06128 and 06129. Geochimica et Cosmochimica Acta 74, 1172–1199. URL: https://www.sciencedirect.com/science/article/pii/S0016703709006681, doi:https://doi.org/10.1016/j.gca.2009.10.029.

Shields, A., 1936. Anwendung der aehnlichkeitsmechanik und der turbulenzforschung auf die geschiebebewegung, mitteilung preussischen versuchsanstalt wasserbau schiffbau [application of similarity mechanics and turbulence research on shear flow]. Preussischen Versuchsanstalt für Wasserbau und Schiffbau, Berlin 26.

Solomatov, V., 2000. Fluid dynamics of a terrestrial magma ocean. Origin of the Earth and Moon 1.

Solomatov, V.S., 1995. Scaling of temperature- and stress-dependent viscosity convection. Physics of Fluids 7, 266–274. URL: https://doi.org/10.1063/1.868624, doi:10.1063/1.868624, arXiv:https://doi.org/10.1063/1.868624.

Sossi, P.A., Klemme, S., O'Neill, H.S.C., Berndt, J., Moynier, F., 2019. Evaporation of moderately volatile elements from silicate melts: experiments and theory. Geochimica et Cosmochimica Acta 260, 204–231.

Spiegelman, M., Kelemen, P., Aharonov, E., 2001. Causes and consequences of flow organization during melt transport: The reaction infiltration instability in compactible media. Journal of Geophysical Research: Solid Earth 106, 2061–2077. URL: https://agupubs.onlinelibrary.wiley.com/doi/abs/10.1029/2000JB900240, doi:https://doi.org/10.1029/2000JB900240, arXiv:https://agupubs.onlinelibrary.wiley.com/doi/pdf/10.1029/2000JB900240.

Spitzer, F., Burkhardt, C., Nimmo, F., Kleine, T., 2021. Nucleosynthetic pt isotope anomalies and the hf-w chronology of core formation in inner and outer solar system planetesimals. Earth and Planetary Science Letters 576, 117211. URL: https://www.sciencedirect.com/science/article/pii/S0012821X21004660, doi:https://doi.org/10.1016/j.epsl.2021.117211.

Srinivasan, P., Dunlap, D., Agee, C., Wadhwa, M., Coleff, D., Ziegler, K., Zeigler, R., McCubbin, F., 2018. Silica-rich volcanism in the early solar system dated at 4.565 ga. Nature Communications 9, 3036. URL: https://doi.org/10.1038/s41467-018-05501-0, doi:10.1038/s41467-018-05501-0.

Sturtz, C., Kaminski, E., Limare, A., Tait, S., 2021a. The fate of particles in a volumetrically heated convective fluid at high prandtl number. Journal of Fluid Mechanics 929, A28. doi:10.1017/jfm.2021.862.

Sturtz, C., Limare, A., Tait, S., Kaminski, É., 2021b. Birth and decline of magma oceans. part 1: erosion and deposition of crystal layers in evolving magmatic reservoirs. arXiv:2108.00910.

Sturtz, C., Limare, A., Tait, S., Kaminski, É., 2021c. Birth and decline of magma oceans. part 2: wobbling thermal history of early accreted planetesimals. arXiv:2108.00995.

Tang, H., Dauphas, N., 2012. Abundance, distribution, and origin of 60fe in the solar plrotoplanetary disk. Earth and Planetary Science Letters 359-360, 248–263.

Taylor, S.R., 1989. Growth of planetary crusts. Tectonophysics 161, 147–156. URL: https://www.sciencedirect.com/science/article/pii/0040195189901510, doi:https://doi.org/10.1016/0040-1951(89)90151-0. growth of the continental crust.

Tkalcec, B., Golabek, G., Brenker, F., 2013. Solid-state plastic deformation in the dynamic interior of a differentiated asteroid. Nature Geoscience 6, 93–97.

Visser, R.G., Ormel, C.W., 2016. On the growth of pebble-accreting planetesimals. Astron. Astrophys. 586, A66, 1–11.

Warren, P., 1985. The magma ocean concept and lunar evolution. Ann. Rev. Earth Planet. Sci. 13, 201–240.

Weidenschilling, S., 1977. Aerodynamics of solid bodies in the solar nebula. Monthly Notices of the Royal Astronomical Society 180, 57–70. doi:10.1093/mnras/180.2.57.

Weisberg, M.K., Boesenberg, J.S., Kozhushko, G., Prinz, M., Clayton, R.N., Mayeda, T.K., 1995. EH3 and EL3 Chondrites: A Petrologic-Oxygen Isotopic Study, in: Lunar and Planetary Science Conference, p. 1481.

Weiss, B., Elkins-Tanton, L., 2013. Differentiated planetesimals and the parent bodies of chondrites. Annual Review of Earth and Planetary Sciences 41, 529–560. URL: https://doi.org/10.1146/annurev-earth-040610-133520, doi:10.1146/annurev-earth-040610-133520, arXiv:https://doi.org/10.1146/annurev-earth-040610-133520.

Wood, J., Dickey, J., Marvin, U., Powell, B., 1970. Lunar anorthosites and a geophysical model of the moon, in: Proceedings of the Apollo 11 Lunar Science Conference, pp. 965–988.

Young, E., Shahar, A., Nimmo, F., Schlichting, H., Schauble, E., Tang, H., Labidi, J., 2019. Near-equilibrium isotope fractionation during planetesimal evaporation. Icarus 323, 1–15.